12-2016

Thermal transport in lithium ion batteries: An experimental investigation of interfaces and granular materials

Aalok Jaisheela Uday Gaitonde
Purdue University

Graduate School Form
30 Updated 12/26/2015

PURDUE UNIVERSITY
GRADUATE SCHOOL
Thesis/Dissertation Acceptance

This is to certify that the thesis/dissertation prepared

By Aalok Jaisheela Uday Gaitonde

Entitled

THERMAL TRANSPORT IN LITHIUM ION BATTERIES: AN EXPERIMENTAL INVESTIGATION OF INTERFACES AND GRANULAR MATERIALS

For the degree of Master of Science in Mechanical Engineering

Is approved by the final examining committee:

Amy M. Marconnet
Chair

Liang Pan

Timothy M. Fisher

To the best of my knowledge and as understood by the student in the Thesis/Dissertation Agreement, Publication Delay, and Certification Disclaimer (Graduate School Form 32), this thesis/dissertation adheres to the provisions of Purdue University's "Policy of Integrity in Research" and the use of copyright material.

Approved by Major Professor(s): Amy M. Marconnet

Approved by: Jay P. Gore 12/2/2016

Head of the Departmental Graduate Program Date

THERMAL TRANSPORT IN LITHIUM ION BATTERIES: AN EXPERIMENTAL INVESTIGATION OF INTERFACES AND GRANULAR MATERIALS

A Thesis

Submitted to the Faculty

of

Purdue University

by

Aalok Jaisheela Uday Gaitonde

In Partial Fulfillment of the

Requirements for the Degree

of

Master of Science in Mechanical Engineering

December 2016

Purdue University

West Lafayette, Indiana

To my family and friends (both furry and otherwise)

ACKNOWLEDGMENTS

This thesis would not have been possible without the support and encouragement from my adviser Dr. Amy Marconnet. She has been supportive since I began working with her on a short project in the summer of 2015, which ultimately led to a Masters thesis. I am deeply indebted to her for the countless skills and qualities that she has passed on to her students like me, and my lab mates. It is only because of the confidence that she has shown in me, in her methodical approach towards research, courteous nature, flexibility, and candor, that I have truly and thoroughly enjoyed working at her Marconnet Thermal and Energy Conversion Laboratory for the past year and a half. I also thank her for her extremely detailed feedback and help during the editorial process of this thesis and other papers. It has been a very humbling experience.

I am grateful to my first academic adviser Dr. Liang Pan, for his support and guidance on course selection when I was a new incoming graduate student at Purdue, and also for later serving on my thesis committee. I would also like to thank Dr. Timothy Fisher, for his collaboration, time, guidance, advice, and serving as on my defense committee. It has been pleasurable working with you, and also taking classes with you. I appreciate his love for the 'motherland'. I am also very thankful to Dr. Jim Jones, whom I have enjoyed working with as a Graduate Teaching Assistant for the past year and a half, where I had an opportunity to teach and mentor one of Purdue's largest classes.

I also thank all the support staff at the School of Mechanical Engineering and at the Birck Nanotechnology Center, that has made my research smooth and productive, especially Holly McIntire, Shana Bordner and Jill Clausen for placing and approving countless orders for me, Jennifer Scruggs for making sure that I get my stipend on time, and Rick DuVall, Adrian Matlock, Mary Jo Totten and Kyle Corwin for

handling the logistics, receiving and getting to me the tons of material (sometimes very heavy and bulky) that I have had to order over the course of my projects.

It has also been a great experience collaborating with Rajath Kantharaj, Ishan Srivastava and Amulya Nimmagadda, this research would not have been possible without their help and support. I would also like to thank my lab mates and friends Yash Ganatra and Collier Miers for their witty inputs, thoughts and constructive feedback on my research, designs, experiments, numerical codes, and even while navigating rigorous grad classes that we took together. I would also like to thank my fellow graduate students Shashank Sarbada and Pooja Shah for their friendship, support, and keeping company often at crazy unearthly hours.

I thank my parents Jaisheela and Uday, big sister Ulka, for their sacrifices and efforts in supporting me through grad school (and while I was busy in the lab, keeping up for weeks with my mode of communication - text messages). I also appreciate the mental company of my four legged furry friends back home in India, many of whom now rest in peace in canine heaven. Among other canines and felines, Ronaldo and Cheeto keep providing much needed distraction and comfort during the long lab hours, by means of their pictures and videos sent across by their humans, and my friends, Swarup and Ashwin.

I would also like to thank Steven Titolo, Thermophysical Properties Research Laboratory (TPRL), for providing crucial feedback on my prototypical designs, and fabricating some intricate test setups. Finally, I would also like to thank and acknowledge Steve Rickman, NASA Technical Fellow, Langley Research Center at NASA, for providing guidance and insights on the ISS Battery Thermal Management project. Funding from NASA/AMA for the purchase of equipment and supplies for a part of my research is gratefully acknowledged.

TABLE OF CONTENTS

Page

LIST OF FIGURES

Figure Page

Figure Page

Figure Page

Figure Page

ABSTRACT

Gaitonde, Aalok Jaisheela Uday M.S.M.E, Purdue University, December 2016. Thermal Transport in Lithium Ion Batteries: An Experimental Investigation of Interfaces and Granular Materials. Major Professor: Amy M. Marconnet, School of Mechanical Engineering.

Increasing usage and recent accidents due to lithium-ion (Li-ion) batteries exploding or catching on fire has inspired research on the characterization and thermal management of these batteries. In cylindrical 18650 cells, heat generated during the battery's charge/discharge cycle is poorly dissipated to the surrounding through its metallic case due to the poor thermal conductivity of the jelly roll, which is spirally wound with many interfaces between electrodes and the polymeric separator. This work presents a technique to measure the thermal conduction across the metallic case-plastic separator interface, which ultimately limits heat transfer out of the jelly roll.

The polymeric separator and metallic case are harvested from discharged commercial 18650 battery cells for thermal testing. A miniaturized version of the reference bar method enables measurements of the interface resistance between the case and the separator by establishing a temperature gradient across a multilayer stack consisting of two reference layers of known thermal conductivity and the case-separator sample. The case-separator interfacial conductance is reported for a range of case temperatures and interface pressures. The mean thermal conductance across the case-separator interface is 670$\pm$275 W/(m^{2}K) and no significant temperature or pressure dependence is observed. The effective thermal conductivity of the battery stack is measured to be 0.27 W/m/K and 0.32 W/m/K in linear and radial configurations, respectively.

Many techniques for fabricating battery electrodes involve coating particles of the active materials on metallic current collectors. The impact of mechanical shearing on

the resultant thermal properties of these packed particle beds during the fabrication process has not yet been studied. Thus, the final portion of this thesis designs and validates a measurement system to measure the effects of mechanical shearing on the thermal conductivity of packed granular beds. This system simultaneously shears the sample while applying a temperature gradient across the particle bed, enabling thermal conductivity measurements using a radial equivalent of the conventional reference bar method.

Results of this research, which includes characterization of thermal conductance across the rate limiting separator-case interface, will help improve the design and reliability of lithium ion batteries. Cells of larger dimension and capacity could also be achieved by the improved understanding of thermal transport across the microscopic electrode stack. Better analytic models of the thermal response of the batteries could be constructed, by taking into account the interfacial conductance and thermal conductivity of the electrodes measured in this work. This is of particular importance in the current circumstances, where accidents and safety issues related to lithium ion batteries are on the increase.

CHAPTER 1. INTRODUCTION

Commercially available lithium-ion (Li-ion) batteries have been around since the 1990s, but recent advances in consumer electronics, *viz.* smart phones, laptops, tablet computers, hover boards, etc. have led to an tremendous increase in their usage in the past few years. Li-ion batteries consists of two electrodes, the cathode and the anode, and an electrolyte. Typically, the electrodes are often thin films of copper and aluminum separated by a porous plastic film, generally referred to as the separator, which electrically insulates them from one another, but allows lithium ions to permeate. Often, the cathode is made of a pure lithium oxide, and the anode is made of graphite or carbon. The electrolyte carries the lithium ions which carry charge through the porous separator. When the battery is being charged, the positively charged lithium ions move from the cathode to the graphite structure on the anode through the separator. During discharging, the lithium ions move from the anode to the cathode, while electrons move across the load generating electric current.

These batteries have many advantages over other types such as Lead acid, Nickel-Cadmium, etc. such as high power density, low self-discharge rates, low memory effects, high efficiency, and they can also be packaged into a variety of form factors. This makes them more suitable for portable devices like phones and laptops. Smart phone sales are set to reach up to 2.6 billion units by the year 2019 [1], which will only increase their demand. More recently, Li-ion batteries have also found use in electric vehicles. The United States Environmental Protection Agency (US-EPA) guidelines for NO_x emission norms have seen a decrease of over 95% in the past three decades, and although the conventional IC engine technology is trying to keep up, automobile manufacturers have already started investing in and developing the hybrid and electric vehicles. In the United States, the current market share of electric vehicles is about 1.2% and that in Norway is about 33% [1]. These vehicles have already shown promise,

capability and efficiency, while having no emissions during operation. According to some recent market surveys, the Li-ion battery business is expected to reach over $45 billion [2].

Rechargeable Lithium ion batteries have high volumetric energy density, generally 3 to 5 times greater than lead acid, Ni-Cd, and Ni-MH batteries. This has lead to their widespread use in portable electronics such as laptops, smart phones, and cameras, and, more recently, in hybrid electric vehicles and aircraft [3–6].

Commercially available Li-ion batteries, such as the 18650 cells typically used in laptops, consist of a carbon coated Copper foil, which acts as the negative electrode, an Aluminum foil coated with lithium metal oxides as the positive electrode, an electrically insulating plastic separator film usually made of polypropylene, stacked and rolled together with inside a metallic case with an electrolyte of lithium salts in an organic solvent [7]. Although the electrical performance of Li-ion batteries mainly depends on the electro-chemical reactions at the electrodes, the thermal performance depends on the heat transport across the multifarious interfaces between the different electrodes and the separator.

Although Li-ion batteries offer many advantages, such as low self-discharge rates, low maintenance, and high efficiency, recent events such as the Boeing 787 Dreamliner battery fires, as well as laptops, cell phones, and electric vehicles catching on fire, have generated public concern and motivated the need for a deeper understanding of the thermal behavior of these batteries. A list of 10 such recent incidents is compiled by Wang *et al.* [8]. Driven by the importance of thermal management of Li-ion batteries, considerable research has been done in the past decade [9–14]. AlHallaj *et al.* [3] developed a one dimensional model with lumped parameters for commercially available 18650 cells, in order to evaluate the internal temperature profiles of the battery as a function external cooling rates, for different discharge rates and predict the temperatures at which thermal runway occurs.

More recently, the rate of heat generation during discharge was measured *in situ* for a 26650 battery [15], and it has been reported that at high discharge rates, most

of the heat that is generated by electro-chemical reactions is stored within the cell, in the absence of any active cooling methods. Shah et al. [16] investigated the use of heat pipes passing axially through the cylindrical cells as an active cooling method to conduct heat away from the batteries during operation, yielding a large temperature drop of 18-20 °C at the core of the cell, which helps prevent the batteries from overheating, and their work has also been demonstrated that in the presence of heat pipes passing axially through the center of the battery also prevents the battery from exploding in a thermal runaway situation. Although the benefits of this design are enormous, changing the manufacturing process to incorporate the heat pipes, and management of the heat pipes themselves is a great challenge, given that a electric vehicle generally has over 7000 individual 18650 batteries that make up the entire battery pack.

Due to the numerous electrode-separator interfaces in the radial direction, the effective thermal conductivity is low [12], which limits heat transport from the core to the cell package. Thus, increasing the external heat transfer co-efficient does not always aid in cooling of the core of the battery [9; 16]. Since the heat generated in the cell must ultimately be conducted to the outer case and then to the surroundings, characterization of thermal conductance across the interfaces within the cell is important. Only a few researchers [7; 14; 17] have measured thermal properties and thermal contact resistances of some components within the batteries, such as the cathode-separator interface recently measured by Vishwakarma *et al.* [12]. Although it is critical, little data yet exists for the interfacial thermal resistance between the metallic case of the battery and the jelly roll, which may ultimately limit heat removal from the system.

To address these challenges and evaluate key thermal properties and interface resistances, this thesis consists of the following elements:

1. Chapter 2 discusses a methodology for measuring the thermal conductivity of the individual electrodes, battery stack, and interfacial thermal conductance between the separator and metallic shell (battery case) interface, by harvesting

electrodes from a commercial 18650 cylindrical Lithium ion battery and using a miniaturized version of the conventional reference bar method for thermal conductivity measurement

2. Chapter 3 discusses *in situ* thermal conductivity and conductance measurements of a dry 18650 battery, performed using a custom test rig,similar to a radial version of the conventional reference bar method

3. Chapter 4 discusses design,manufacturing and validation of a cylindrical Taylor-Couette cell to simultaneously apply mechanical shearing forces and a temperature gradient on a bed of packed granular material, to determine the changes in thermal conductivity as a result of the mechanical perturbations

CHAPTER 2. LITHIUM ION BATTERY MEASUREMENTS

Chapter 2 derives from and expands on a journal publication (under review) A. Gaitonde, A. Nimmagadda, A. Marconnet: Measurement of Interfacial Thermal Conductance in Lithium Ion Batteries, in *The Journal of Power Sources*, The International Journal on the Science and Technology of Electrochemical Energy Systems, 2016.

2.1 Introduction

This chapter develops a methodology to measure the interfacial thermal conductance between the polymeric separator and the metallic shell (case) of a commercial 18650 battery cell using a comparative infrared microscopy technique. During the course of this project, it was found that the outermost layer of the jellyroll is the plastic separator, which insulates the jellyroll electrically from the metallic case. As the final layer of jellyroll is the polymeric separator, the interface resistance between it and the case is crucial to the overall heat dissipation in the system. Here, measurements are performed for two configurations, linear and radial. For the linear configuration, the jellyrolls are harvested by dissecting a commercial Lithium ion battery, and samples are prepared for measurement in a cross plane heat transfer measurement rig across a range of temperatures and pressures. Overall, the average measured interfacial thermal conductance is 670 ± 275 W/(m^{2}K), and no significant pressure or temperature dependence is observed. For the radial configuration, 18650 batteries are cut open near the top to expose the top surface of the jellyroll, and are placed in a radial heat transfer measurement rig. This allows for measurements to be performed at various temperatures, with the actual contact pressures.

2.2 Thermal Metrology

2.2.1 Conventional Reference Bar Method

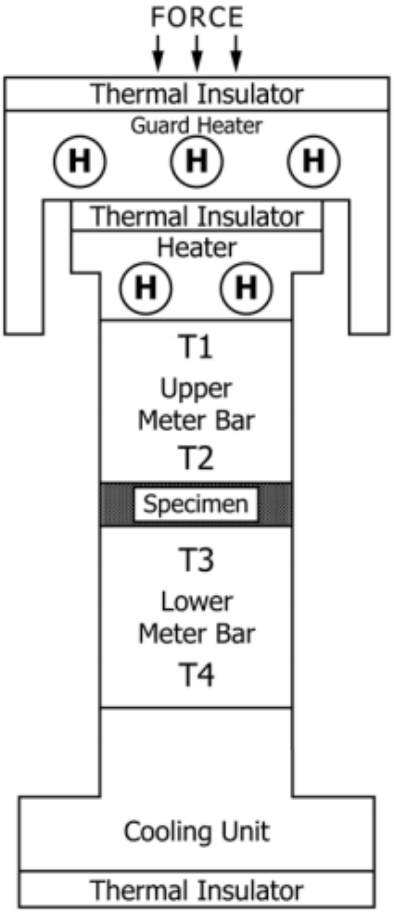

Figure 2.1. The conventional reference bar method based on the ASTM D5470 Standard for thermal conductivity measurement. Heat flows from the upper meter bar, across the specimen, to the lower meter bar. Temperature measurements are taken along discrete points along the meter bars, and are extrapolated to the specimen to calculate the temperature drop in the specimen. This conventional method cannot separate the thermal contact resistance and the intrinsic thermal conductivity of the sample in one measurement. Image reproduced with permission from ASTM [18].

Figure 2.1 shows the schematic of a conventional reference bar method based on the ASTM D5470-12 Standard Test Method for Thermal Transmission Properties of Thermally Conductive Electrical Insulation Materials [18]. Heat generated on the top side heater conducts through the upper reference meter bar, across the sample, to a cooling unit, though the lower reference meter bar. Temperatures are recorded at a few discrete points along the reference or meter bars using thermocouples. A set of thermocouples in the reference (meter) bars are used to quantify the heat flux going through the sample, by calculating the temperature gradient. This temperature gradient is then extrapolated to the edge of the sample to calculate the temperature drop in the sample. A drawback of this method is that it cannot separate the interfacial contact resistance between the two faces of the sample and the reference bars from the thermal conductivity of the sample in one measurement.

2.2.2 Comparative Infrared Thermal Imaging

To address the drawback of the conventional reference bar method discusses in the previous Section 2.2.1, here infrared thermal microscopy is combined with the reference bar method to improve the spatial resolution of temperature measurement, and enable separation of the interfacial thermal contact resistance from the intrinsic thermal conductivity of the specimen [19; 20]. In this work, an infrared microscope (Quantum Focus Instruments (QFI), Vista, CA) has been used extensively to measure thermal conductivity and interfacial thermal conductance. The IR microscope enables accurate temperature mapping with an accuracy of 0.1 [K], up to 1.7 μm with the high magnification (20x) objective lens and a field of view of 0.61mm x 0.61mm. At lower magnification, the 1x lens resolves 11.7 μm at a field of view of 12.3mm x 12.3mm. The 4x objective lens resolves 5μm with a field of view of 3.07mm x 3.07mm. All temperature images are 2D thermal maps with $(1024)^2$ temperature data points.

Based to the conventional reference bar method (discussed in Section 2.2.1), the MTEC laboratory has miniaturized the conventional reference bar method for usage

with the IR Microscope, as shown in Figure 2.2. The setup consists of a hot side adapter plate (H), a cold side adapter plate (C), a 'water block (WB)' and a load cell (LC). The sample to be measured is placed between the hot and the cold adapter plates, and a temperature gradient is created across the sample. The 'water block' is a heat exchanger through which a heat transfer fluid is circulated to maintain a cold side temperature. The load cell measures the force that is applied on the sample through the hot side adapter plate, by means of a rotating micrometer screw gauge. Aluminum bars extend from the hot and cold side adapter plates and match the cross-section of the sample to ensure 1-D heat conduction. The 'The reference bars' in the conventional measurement are shrunk to $\sim$ 1mm thick reference layers integrated in a 'reference-sample-reference' stack. To create a temperature gradient across the sample, one adapter plate is heated, while the other is cooled. Three 60 Watt, 1.5" long cartridge heaters of a diameter of 1/8" are inserted into the hot side adapter plate. The heat transfer fluid flowing through the 'Water Block', connected to the cold side adapter plate, is kept at a set temperature by a Polyscience AD07R constant temperature fluid circulator. The reference layers, which are used to quantify heat flux are very thin, *i.e.*, of the order of magnitude of a few microns to approximately 1mm. The thickness of the reference layers is selected by matching the approximate thermal resistance of the sample estimated from the predicted thermal conductivity of the sample. The thermal resistance, R", of the reference and the sample with unknown thermal properties, needs to be of the same order of magnitude for a comparative analysis of the temperature gradients in the respective regions, so that the temperature gradients (slopes) in the reference region and the sample region can be resolved accurately. The temperature gradient in the sample region, along with the calculated heat flux from the reference region is used to quantify the thermal conductivity of the sample.

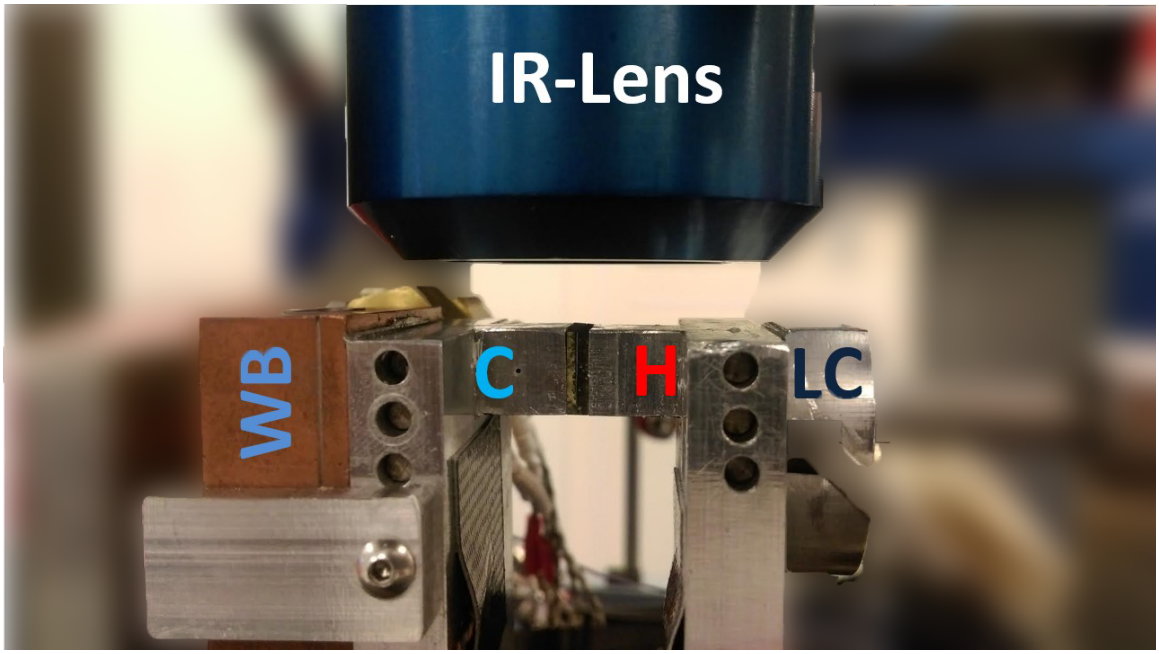

Figure 2.2. Miniature IR Reference Bar Setup. The sample stack is sandwiched between hot (H) and cold (C) side adapter plates. The cold side is attached to the temperature-controlled water block (WB). The hot side temperature is controlled with cartridge heaters embedded in the hot side adapter plate. A load cell (LC) measures the force applied to the sample stack. When a temperature gradient is applied, the IR microscope measures a 2D temperature map of the top surface of the sample stack.

Emissivity Calibration

Prior to the thermal gradient measurement described in the previous section (Section 2.2.2), the first step in the measurement process is the emissivity calibration. The entire sample is heated to an elevated uniform temperature of around 65 °Cusing heaters embedded in both the cold and hot side adapter plates. At this uniform temperature, the (spatially varying) radiance from the reference-sample-reference stack is recorded as a 'Reference Map'. This is then compared to the radiance with that of a blackbody at the same temperature (accounting for effects of reflectivity as well), and emissivity is calculated at each pixel of the sample stack.

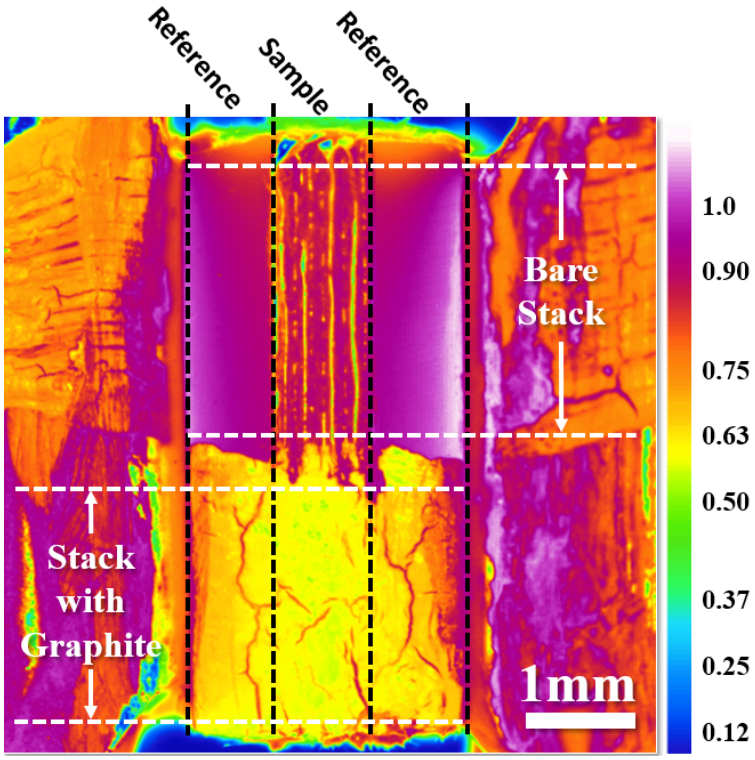

Figure 2.3. A representative emissivity map of a battery stack sandwiched between two acrylic reference layers. As expected, the metallic (aluminum and copper) current collectors in the cathode and anode show very low emissivity. The bottom half of the stack is coated with a very thin layer of graphite to improve the emissivity uniformity of the sample stack.

From Fourier's Law of heat conduction, the heat flux through the reference-sample-reference stack is calculated as

$$q" = k_{ref} \left.\frac{dT}{dx}\right|_{ref} \tag{2.1}$$

$$= k_{sample} \left.\frac{dT}{dx}\right|_{sample} \tag{2.2}$$

where $q"$ is the heat flux, k is the thermal conductivity, $\frac{dT}{dx}$ is the temperature gradient, and the subscripts 'sample' and 'ref' refer to the sample and reference, respectively.

From Equations (2.1) and (2.2), the thermal conductivity of the sample is calculated as,

$$k_{sample} = \frac{q"}{\left.\frac{dT}{dx}\right|_{sample}} = \frac{k_{ref}\left.\frac{dT}{dx}\right|_{ref}}{\left.\frac{dT}{dx}\right|_{sample}}. \tag{2.3}$$

2.3 Fabrication of Battery Samples

Two of the most commonly used lithium ion battery configurations are the pouch cell [21] and the cylindrical battery [22]. Cylindrical cells are widely used in consumer electronics like laptop computers, hover-boards, robotics and remote controlled aircraft or drones. These batteries are also used in electric vehicles, in which they are connected in a combination of series and parallel to up a battery pack of a large capacity. The battery consists of many layers stacked together and permeated with an electrolyte. The electrolyte degrades in air and can form toxic gasses, thus, initial experiments are performed on dry as received battery materials from MTI Corporation. After the sample preparation technique and measurement technique were validated, material was harvested from commercially available 18650 cells.

2.3.1 Constructing a Battery using Dry Electrodes

A dry battery stack is constructed using components of the battery, without any electrolyte, since the measurements are to be performed in the presence of ambient air. The cathode, anode and separator used in 18650 batteries were bought from MTI Corporation, Richmond, CA, in the form of planar sheets (see Figure 2.4). The 50μm thick cathode is $LiFePO_4$ coated on a Aluminum foil (current collector) [23], whereas

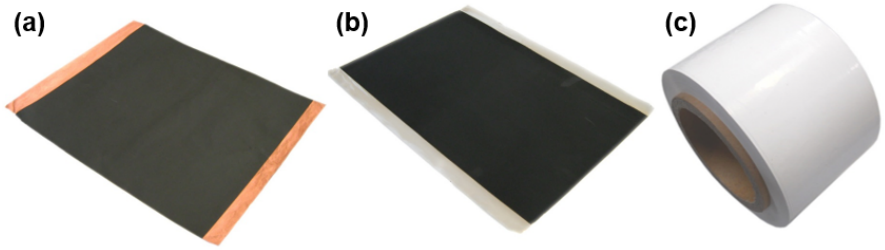

Figure 2.4. Dry Electrodes from MTI Corporation. (a) Anode: Graphite coated Copper Current Collector, (b) Cathode: $LiFePO_4$ coated Aluminum Current Collector, (c) Porous Plastic Separator.

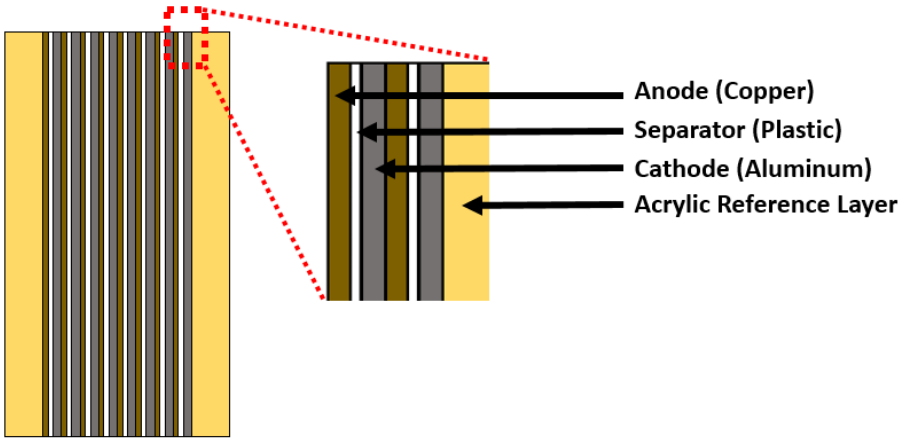

Figure 2.5. Schematic of a dry battery stack as constructed using electrode material from MTI Corporation. The enlarged cutout shows an enlarged portion of the stack consisting of multiple anode-separator-cathode layers.

the 50μm thick anode is graphite coated on a copper current collector [24]. The porous plastic separator film is made from polypropylene, and is 25μm in thickness [25].

The electrodes sheets are 241mm x 200mm in size, and are cut to square 1 cm^2 pieces using a knife for making samples for measurement. The cut square electrodes pieces are then stacked together, with a separator layer between two adjacent electrodes. As shown in Figure 2.5, this stack is then sandwiched between two reference layers of acrylic. For thermal imaging using the IR Microscope, it is very crucial that

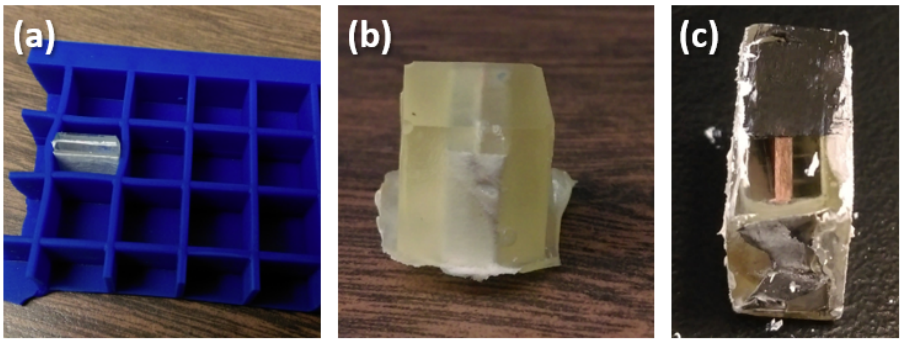

Figure 2.6. Sample preparation procedure: (a) The sample stack, secured in thermal tape, is placed inside a ice cube mold and resin is poured over it, (b) The embedded sample in the hardened acrylic resin, (c) polished imaging surface exposing the battery stack. A thin layer of graphite is applied to increase emissivity.

the top edge of all layers is at the same height, given the very small depth of field of the camera. Initial sample configurations employed high temperature thermally conductive tape to wrap the battery stack together. One edge was polished on a polishing wheel to planarize the imaging surface. However, the layers in the sample stack shifted between polishing and placing in the cross plane rig, making focusing on the sample impossible.

The sample preparation method was subsequently improved using a acrylic resin (Lecoset 100^{TM}, Lecoset Corporation, Michigan City, IN) to hold the sample together during polishing and testing. The resin is a two part mixture, which cures and hardens in air within a few minutes. The sample stack is placed in a mold, and the liquid resin is poured over it. After curing, the embedded sample is removed from the mold, and excess resin is ground off using a polishing wheel of appropriate roughness. The resin arrests any movement of the individual layers between polishing and placing in the rig, but does not penetrate substantially into the reference-sample-reference stack. A very thin layer of colloidal graphite (Ted Pella Inc.) is applied on the polished surface to increase the emissivity of the surface.

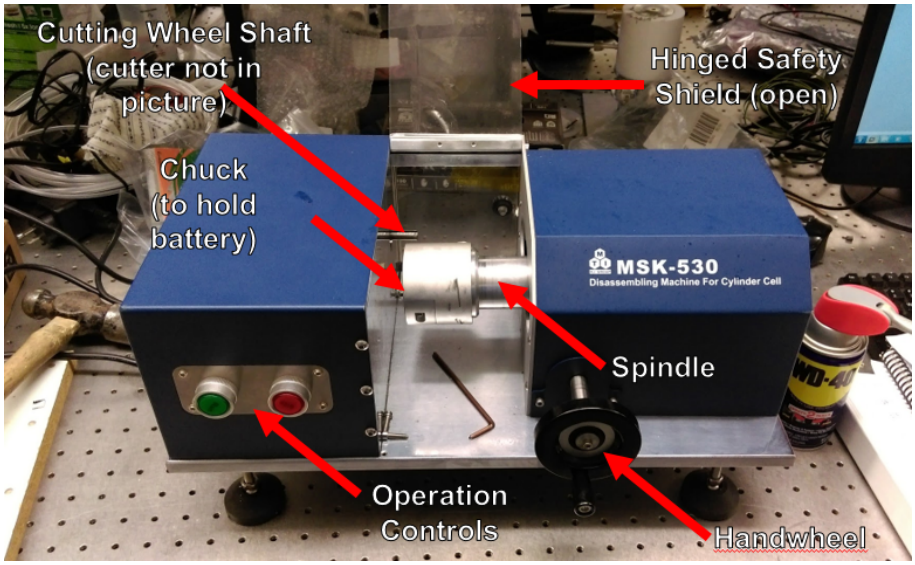

Figure 2.7. The MSK-530 battery disassembly tool which is used to cut commercial 18650 batteries.

2.3.2 Dissecting a Commercial Battery to Harvest Electrodes

A safe battery disassembly procedure has been identified by making use of a MSK-530 Compact Battery Disassembly Machine from MTI Corporation, Richmond, CA. Batteries are discharged to their lowest potential (using a Arbin BT-2000 Battery Testing System) to ensure safety while cutting the batteries (*i.e.*, to prevent a significant current flow, should the battery short during the operation). The battery disassembly tool consists of two motors, which have parallel axes of rotation, offset from each other. This offset can be accurately controlled using a hand-wheel to translate the spindle. One motor rotates a spindle at 1000 RPM, and has a chuck to house a cylindrical 18650 battery. The other motor rotates a 0.2mm thick, 50mm diameter, 128 teeth carbide metal cutting blade at 1000 RPM. The battery is loaded and secured into the chuck, and the hand-wheel is rotated, which moves the spindle towards the cutting blade. Once the battery touches the cutting wheel. A micrometer screw gauge, mounted on the same axis of the hand-wheel, is configured to control the depth of cut of the battery. This depth of cut is set slightly below 200 µm, which

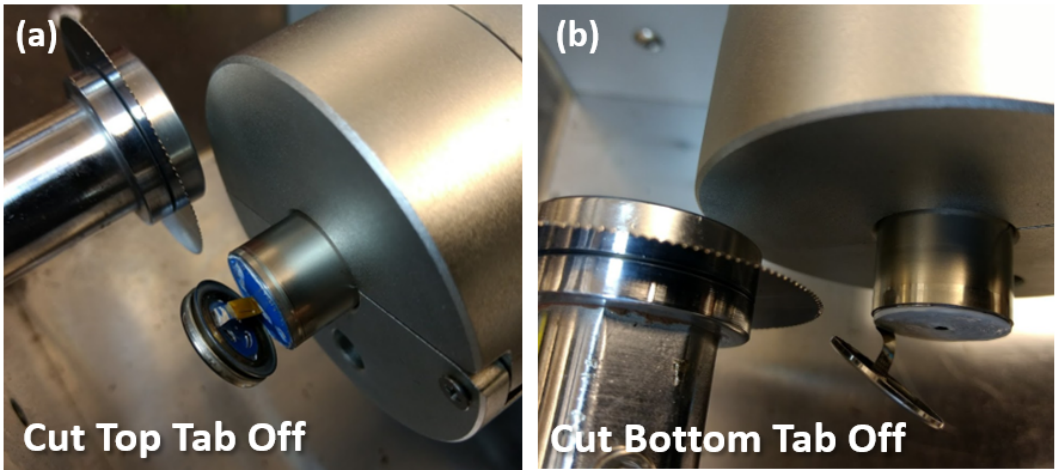

Figure 2.8. Cutting the top and bottom tab off using the MSK-530 Compact Battery Disassembly Tool. The depth of cut is controlled accurately using a micrometer so as to not short the inner electrode layers.

is the thickness of the 18650 case. This is done so that the metallic cutting wheel does not short the case with the electrodes which are wrapped by the separator. Once the depth of cut is set, the hand-wheel is retracted slightly, and the motors are started by operating the control unit of the machine. The spindle is then translated forward carefully to cut the case. Once an incision is made, the final cut is made using a sharp ceramic knife. As shown in Figure 2.8, this procedure is repeated twice, once to cut off the top tab off, near the positive electrode, and then near the bottom face of the battery.

The jellyroll of the battery does not slide out from the metallic shell, even after application of a significant force along the axis of the battery. Hence, a Proxonn 37110 MF70 Micro Mill is used to cut a lateral incision along the length of the battery. This 100 Watt mill has three axes control, and the speed of cutting can be varied from 5,000 to 20,000 RPM. This lateral cut exposes the jellyroll, and a pictorial procedure is shown in Figure 2.9. Metallic dust generated while using the micro-mill is dusted off using a spray of compressed air.

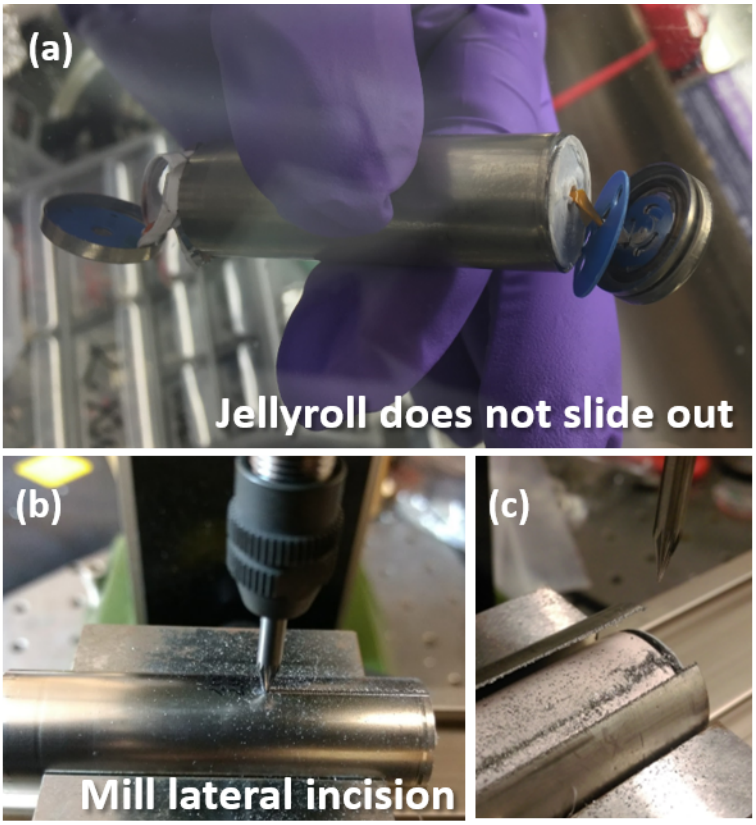

Figure 2.9. (a) The jellyroll does not slide out of the metallic shell after the top and bottom tabs are cut, (b) a micro-milling machine is used to make a lateral incision along the length of the battery, without cutting into the electrode layers below the case, (c) exposing the jellyroll.

The jellyroll is separated from the case, and is put inside an Argon filled glove-box, since the electrolyte in the jellyroll degrades in air. Ceramic tweezers are used to separate the cathode, anode and the separator layers by unrolling the jellyroll, as shown in Figure 2.10(a) and (b). These layers are then stores separately. Dimethyl carbonate (DMC) is used to neutralize and wash the electrolyte off. DMC is poured into a Petri dish, and the electrodes are soaked in the DMC filled Petri dish for a few seconds until the lithium salts are washed off (see Figure 2.10(c)). The wet layers are then removed from the Petri dish, and kept on a clean surface inside the glove-box. The DMC evaporates in the Argon environment, and the dry electrode layers, now

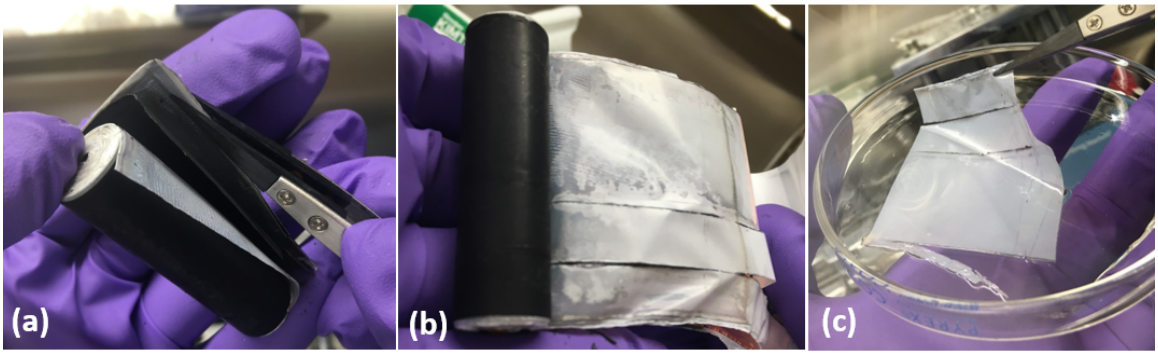

Figure 2.10. (a) The jellyroll is placed inside a Argon filled glove-box after the milling operation is completed. This prevents oxidation or degradation of the electrolyte in the presence of air or oxygen. (b) The layers are separated by unrolling the jellyroll, and (c) the electrolyte is washed off using Di-methyl-carbonate, an organic solvent.

without any electrolyte, are removed from the glove-box, and the same procedure is employed to make the sample stack, as discussed in Section 2.3.1.

2.4 Results and Discussion

This section presents the effective thermal conductivity measurements of the 18650 Li-ion battery, *viz.* the cathode, anode, plastic separator, and the entire battery as a stack.

2.4.1 Cathode

The active material in the cathode is Lithium ferrous phosphate ($LiFePO_4$), which is coated on both sides of a thin Aluminum (Al) foil. The Al foil serves as the current collector. Figure 2.11 shows the cathode sample that is prepared for thermal conductivity measurements. The current collector is measured to be 30µm thick, whereas the average overall thickness of a single layer of cathode is 150µm. The sample consists of 10 layers of the cathode electrode stacked together in parallel. The

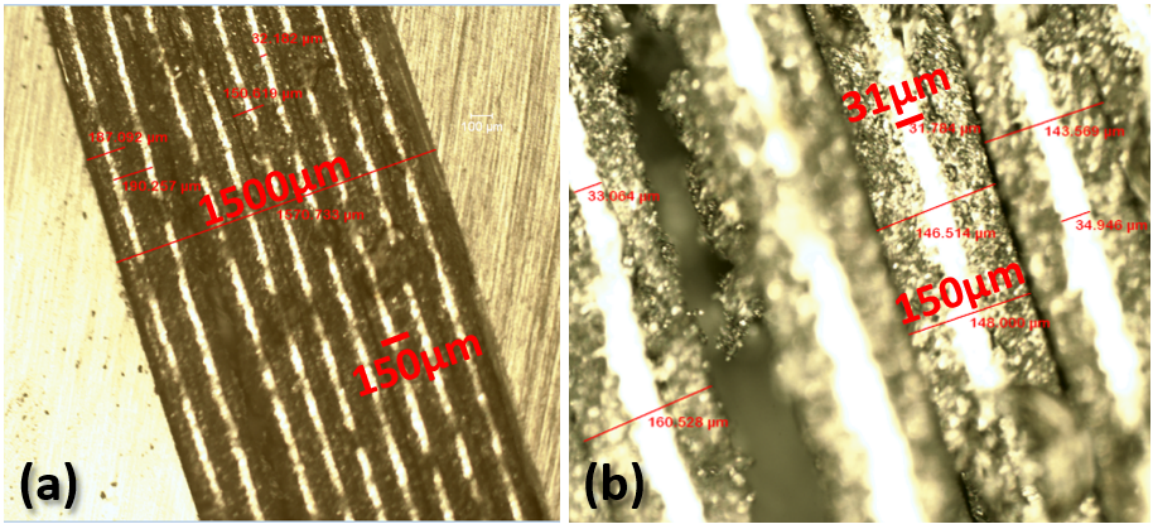

Figure 2.11. Optical images of a stack of cathode layers. (a) Image taken with a 5x objective lens and (b) Image taken with a 20x objective lens.

effective thermal conductivity of the cathode (including the metallic current collector) is measured by using the miniaturized version of the cross plane rig, as discussed in Section 2.2.2.

Figure 2.12 shows the temperature gradient in the cathode sample, as a function of heat flux passing through the sample. The slope of the best fit line then yields the effective thermal conductivity of the cathode. The heat flux levels are varied by adjusting the hot side temperature, while maintaining the cold side temperatures to a fixed value. Data is recorded after the hot side temperature reaches a constant value and the system settles to a steady state. The fitted thermal conductivity of the cathode is calculated to be 0.316 W/m/K. Note that individual layers of the cathode stack are not separately resolved in this measurement, instead this value is an average over the active region, the metal current collectors, and any interfacial effects.

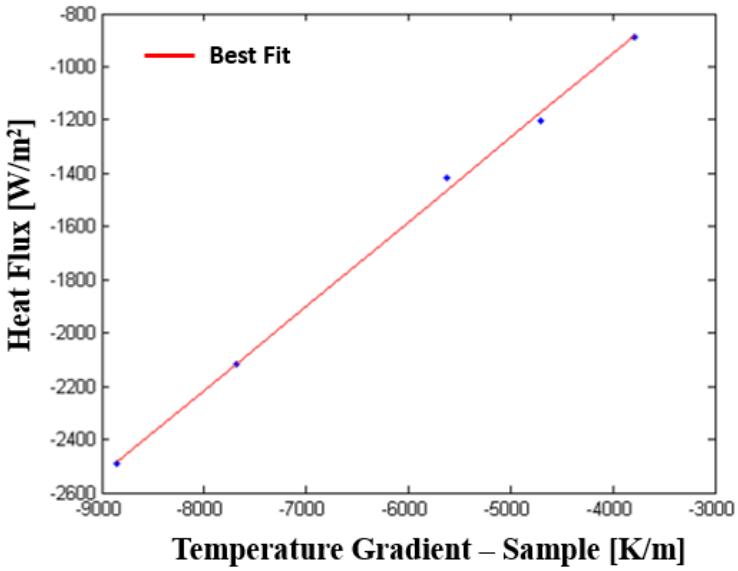

Figure 2.12. Temperature gradient in the cathode stack as a function of heat flux. A linear curve (denoted by the red line) is fitted in the measured values of temperature gradient in the same at discrete heat flux levels (blue dots).

2.4.2 Anode

The anode consists of a copper foil current collector with a graphite coating. Figure 2.13 shows an optical image of the anode stack, and Figure 2.14 shows a 2D temperature map of the sample when a temperature gradient is applied across it, and its corresponding averaged 1D temperature profile. Similar to 2.12, the temperature gradient in the anode stack is plotted as a function of heat flux, and the fitted effective thermal conductivity of the anode stack is calculated to be 0.67 W/m/K. This value incorporates effects of the active electrode materials, the metallic current collectors, and interfaces within the stack.

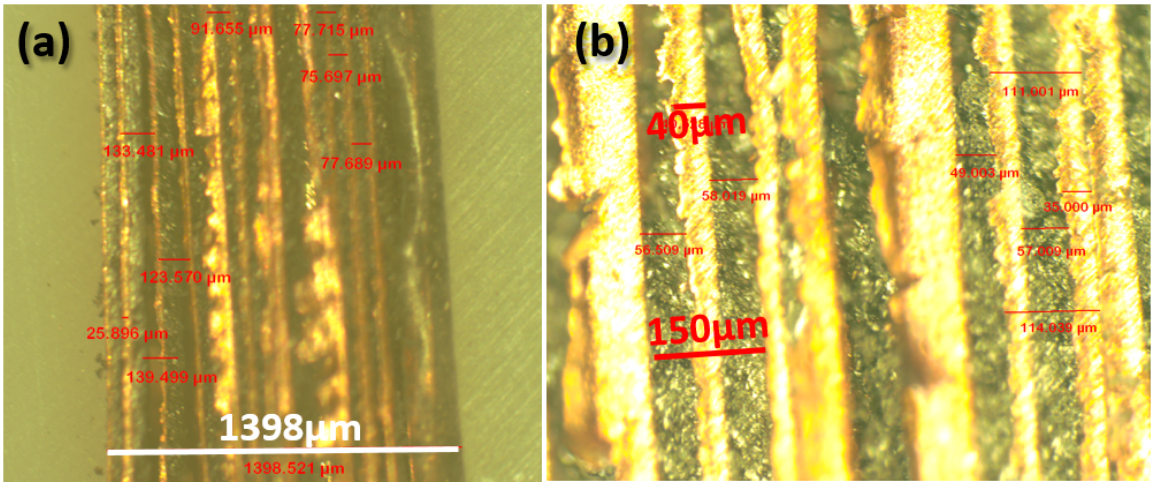

Figure 2.13. Optical images of a stack of anode layers (a) Image taken with a 5x objective lens, and (b) Image taken with a 20x objective lens.

2.4.3 Battery Stack

Figure 2.15(a) shows a optical image of the sample used to measure the effective conductivity of a complete battery stack, as seen from optical microscope with a 20x objective lens. The battery stack is prepared by staking the cathode and anode together, and inserting a layer of the plastic separator in between two successive electrodes. The measured effective thermal conductivity of the battery stack is calculated to be 0.273 W/m/K. Again, this value incorporates effects of the active electrode materials, the metallic current collectors, and interfaces within the stack.

In these measurements, there is no electrolyte since the measurements are conducted in the presence of air, which makes this a dry battery. Addition of the electrolyte will require construction of a inert gas chamber, to prevent oxidation and degradation of the electrolyte. This work is in progress, and a part of it is discussed in further detail in Chapter 3.

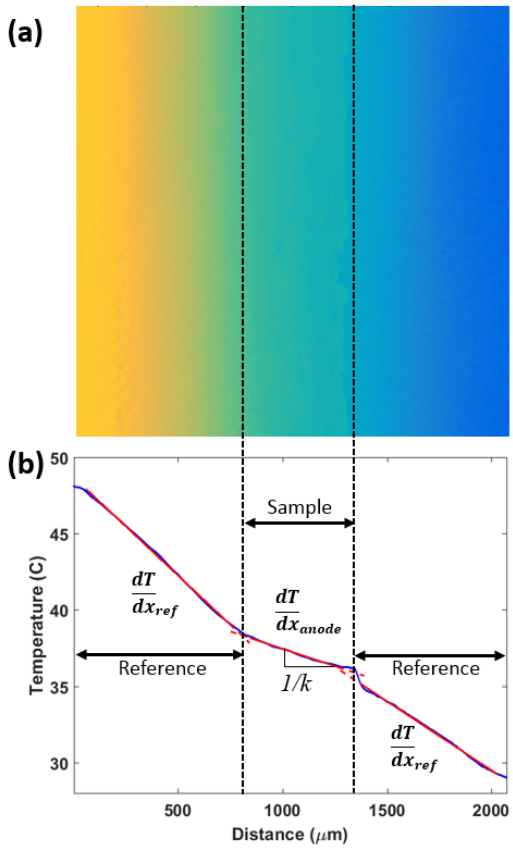

Figure 2.14. (a) A representative 2D temperature map of the PTFE reference-anode stack-PTFE reference, at a specified flux level, and (b) the corresponding averaged 1D temperature profile with the different regions identified. The inverse of the slope of the line in the sample region gives the thermal conductivity of the anode stack.

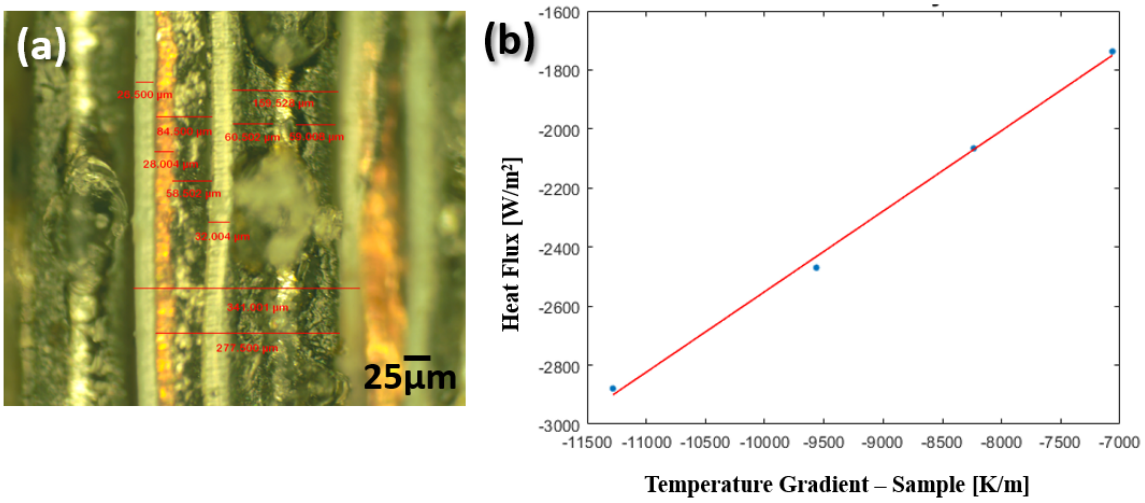

Figure 2.15. (a) Optical image of a battery stack consisting of successive separator-cathode-separator-anode structures, as seen through a 20x objective lens, and (b) the fitted effective thermal conductivity of a dry battery stack.

2.5 Interfacial Conductance Measurements

Since heat generated in the cell (jellyroll) during the electro-chemical reactions during operation must ultimately be conducted to the outer case and then to the surroundings, characterization of thermal conductance across the interface of the final layer of the jellyroll and the metallic case is important.

As previously discussed in Chapter 1, few measurements exist [7; 14; 17] on thermal properties and thermal contact resistances of the components within batteries. Recently, the cathode-separator interface was measured by Vishwakarma *et al.* [12]. But little data yet exists for the interfacial thermal conductance between the metallic case of the battery and the jelly roll, which may ultimately limit heat removal from the system.

Here, the sample stack consists of a hot side reference layer, separator layers, the 18650 metallic case, separator layers, and a cold side reference layer as shown in Figure 2.16 (c). This symmetric structure enables measurement of the two case-separator interfaces (on either side of the case) during a single test. Several separator layers are placed on either side of the case to better resolve the temperature profile in the separator region. Prior to each temperature measurement, the spatially dependent emissivity is calibrated by uniformly heating the sample to a known temperature and measuring the radiant power.

While the temperature gradient is applied, the IR microscope measures a 2-D temperature map, which is then averaged in direction normal to the heat flow path to generate a 1-D temperature profile (see Figure 2.16). Based on the slope of the temperature profile in the reference region, the heat flux is quantified with Fourier's law. Note that the thermal conductivity of the black PTFE reference material is verified against gum rubber, a Standard Reference Material certified by the National Institute of Standards and Technology (NIST). As shown in Figure 2.16 , the temperature jump at the left and right interface can be identified from the 1D temperature profile, denoted by ΔT_{left} and ΔT_{right}.

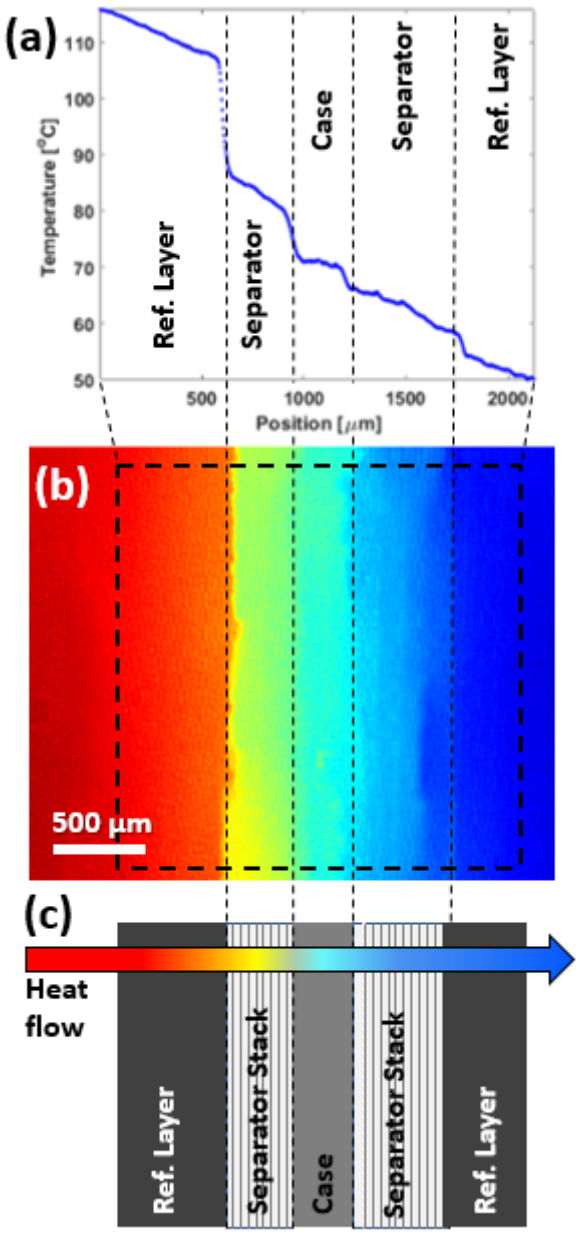

Figure 2.16. (a) A representative, averaged 1D temperature map, and (b) the corresponding 2D temperature profile showing the temperatures and gradients in the different regions of the sample stack (c). The 1D temperature profile shows no temperature drop in the case, due to its thermal conductivity being an order of magnitude higher than that of the separator or reference material.

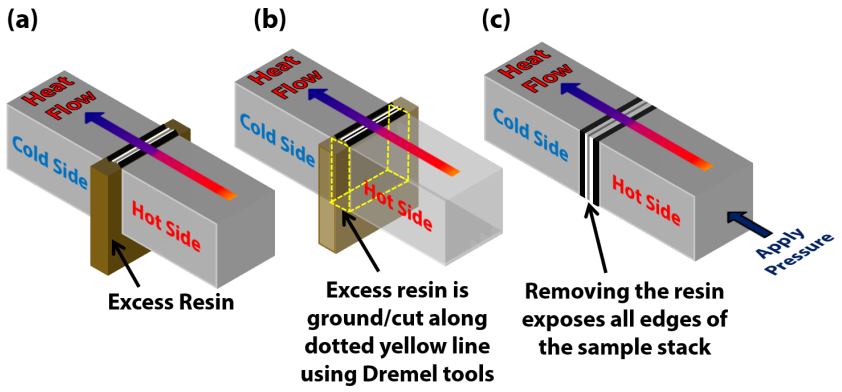

Figure 2.17. (a) An over-sized sample with one polished edge with resin on the other three edges is placed between the jaws of the cross plane measurement rig, (b) excess resin is ground/cut off using suitable Dremel^{TM} tools, and (c) the sample stack is held between the jaws without any resin. Pressure is now adjusted using a load cell.

Combining these measurement, the thermal conductance, G, is calculated from

$$G = \frac{1}{R"} = \frac{k_{ref}\frac{dT}{dx}_{ref,avg}}{\Delta T}. \tag{2.4}$$

For each cold side temperature, four temperature maps at different heat flux levels are measured. This enable simultaneous evaluation of an average fitted interface conductance based on Ohms Law for Thermal Resistances:

$$\Delta T = q" R" = \frac{q"}{G}. \tag{2.5}$$

Specifically, the thermal resistance is the slope of the temperature jump as a function of heat flux (see Figure 2.18), and the conductance is simply the inverse of the slope.

For thermal analysis, the separator material and the metallic case are sandwiched between two layers of a known reference material, black polytertrafluroethylene (PTFE), which is opaque to IR and has a high melting point (>326°C). One edge of the sample stack (consisting of the hot side reference layer, separator layers, 18650 metallic case, separator layers, and cold side reference layer, see Figure 2.16) must be polished in order to enable a flat surface for thermal imaging (it is crucial that the top surface of the sample is planar due to the depth of focus of the IR microscope). To

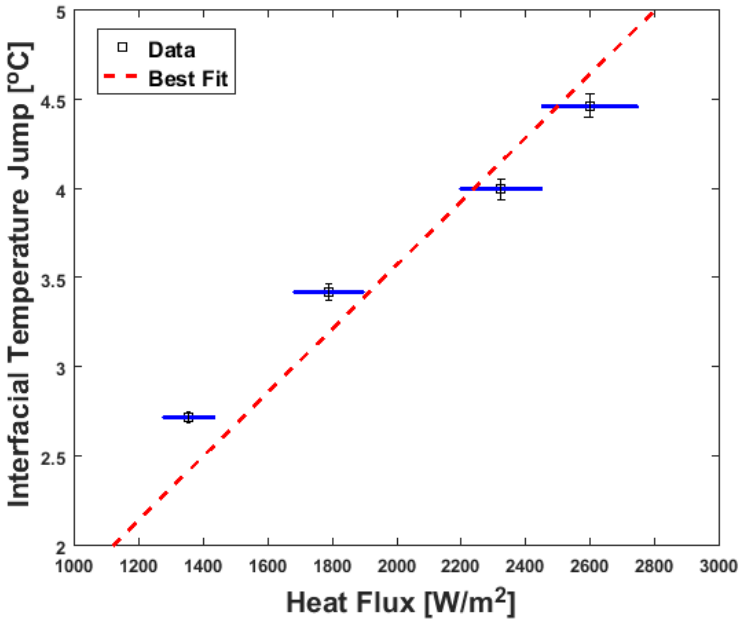

Figure 2.18. Interfacial temperature jump as a function of applied heat flux for a sample with a cold side temperature of 90°C. The fitted thermal resistance of the interface is the slope of the fitted line.

enable polishing, the sample stack is temporarily held together with an acrylic resin (Lecoset 100^{TM}) at the edges of the oversize sample stack. After polishing and after the sample is mounted and secured in the measurement rig, excess resin is ground off using a Dremel^{TM} tool to enable pressure dependent tests.

Here, the interfacial thermal resistance between the polymeric separator and the case of a commercial 18650 battery cell is measured using a comparative infrared microscopy technique across a range of temperatures and pressures relevant to operation. As the outermost layer of jellyroll is typically the polymeric separator, this interface resistance is crucial to the overall heat dissipation in the system. Overall, the average measured interfacial thermal conductance is 670 $\pm$ 275 W/(m^{2}K), and no significant pressure or temperature dependence is observed.

2.6 Results and Discussion

Eight interfaces are measured across a range of temperatures (35-120°C) and pressures (0.1-0.25 MPa). Across all measured temperatures and pressures, the mean thermal conductance between the case and the separator is 670 W/(m^{2}K) with a standard deviation of 275 W/(m^{2}K). This magnitude is comparable to the thermal conductance of 300 μm of polymer (approximately 10-15 layers of the separator). As illustrated in the following sections, no clear temperature or pressure dependence is observed, but large sample-to-sample variations are evident.

2.6.1 Temperature Response

Here, the temperature of the metallic case is used as the metric for classifying temperature dependence. Case temperatures are indirectly controlled by setting the high side and low side boundary temperatures. Note that the thermal resistance (L/k) of the case itself is quite small. Thus, the temperature drop across the case is negligible.

Experiments for higher case temperatures (between 80°C and 120°C) required relatively low heat flux levels, since the high side temperature was limited to 130°C (the melting point of the separator). Variations in data at the same case temperature (e.g. 100°C) for the same sample are due to the different heat flux levels required to achieve the case temperature with different cold side temperatures.

Figure 2.19 (a) illustrates the thermal conductance for 4 interfaces tested in the range of 60-80°C across all pressure levels (0.1-0.25 MPa). Figure 2.19(b) illustrates the thermal conductance for all 8 interfaces tested in the range of 35-120°C across all pressure levels (0.1-0.25 MPa). As illustrated by the overlapping data, although much variation between individual trials is observed, there is no clear temperature or pressure dependence. Binning the data into 2°C and 5°C windows, for the narrow and wide data ranges in temperature, yields the averaged data curve shown in Figure 2.19 (a). Although a slight increase in thermal conductance at low temperatures is

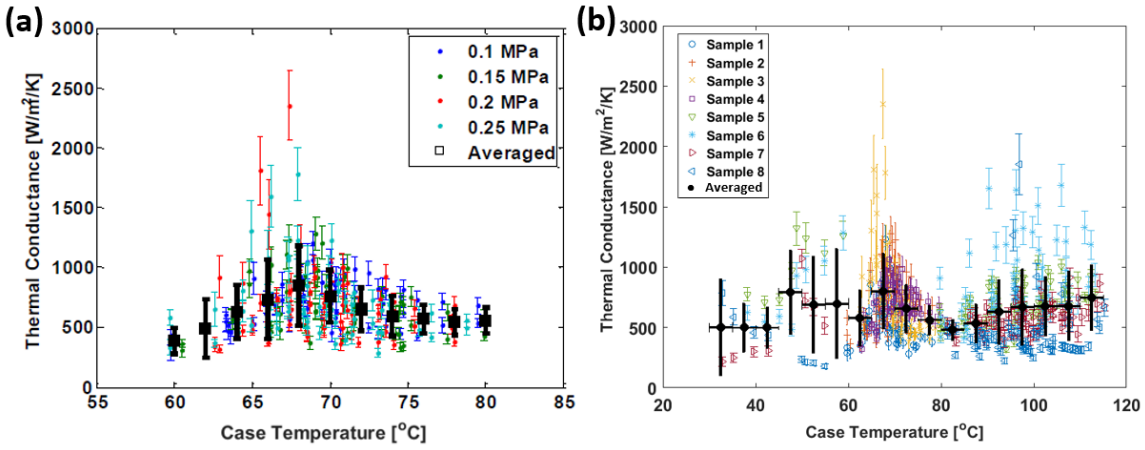

Figure 2.19. (a) Thermal conductance as a function of temperature for interfaces 1-4 with pressures from 0.1 to 0.25 MPa. Circles indicate individual measurements and the error bars are the uncertainty in those individual data points. The bolded square symbols indicate the average measured thermal conductance for bins of width 2°C centered at the marked temperature location. The error bars on these binned averages represent the standard deviation of measurements within the given temperature bin. There is no statistical significant variation in the measured interface conductance with temperature in this range, (b) Thermal conductance as a function of temperature for all 8 interfaces across all pressures. Colored symbols indicate individual measurements and the error bars are the uncertainty in those individual data points. The black bolded circles indicate the average measured thermal conductance for bins of width 5 °C centered at the marked temperature location. The error bars on these binned averages represent the standard deviation of measurement within the given temperature bin. There is no statistical significant variation in the measured interface conductance with temperature.

observed in these mean values, it is not statistically significant given the variation from trial to trial.

2.6.2 Pressure Response

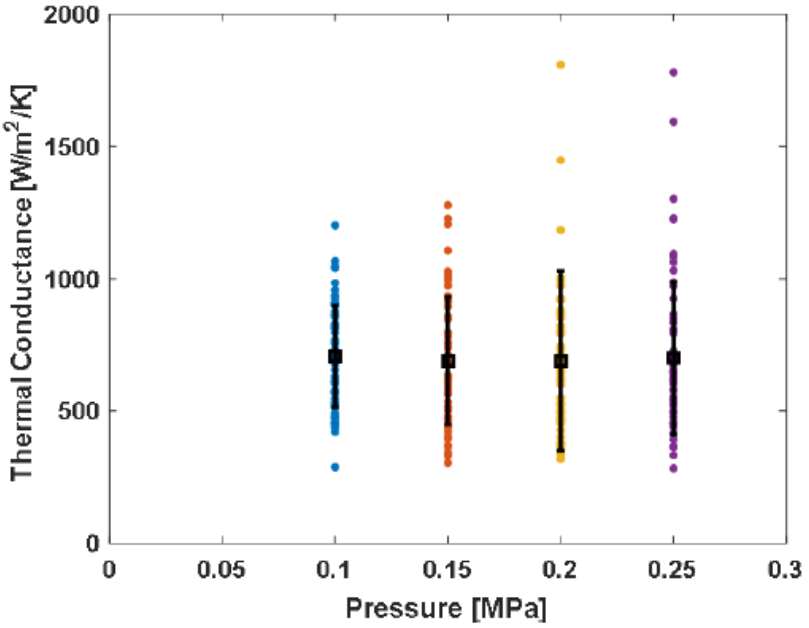

Figure 2.20. Thermal conductance as a function of pressure for 4 interfaces with case temperatures in the range of 60-80°C.

Figure 2.20 shows all values of thermal conductance at all pressure settings for the four interfaces tested in the range of 60-80°C. Although there are a few trials which show higher conductance at higher pressures, the mean of all samples at the given conditions is constant at 700 W/(m^{2}K) across all pressures. While an increase in contact conductance was expected, due to improved physical contact between the separator and the case with increasing pressure, based on the data, the range of pressures is too small for this effect to be significant.

2.7 Conclusions

With increasing usage of Li-ion batteries, safety concerns are on the rise, and most failures or accidents reported are due to thermal effects such as poor heat dissipation from the core of the battery to the outer case leading to thermal runaway. In this work, the first measurements of the thermal conductance across the final layer of the jelly roll, which is the separator, and the metallic case are reported. Our infrared microscopy technique allows accurate *in situ* temperature mapping across the case-separator interface with a high spatial resolution of upto 1.7μm. Experiments have been carried out for case temperatures of 35-120°C, between a pressure range of 0.1-0.25MPa for each case temperature. Although the conductance across the case-separator interface is expected to increase with pressure due to improved contact, measurements carried out in this work do not show this trend. The measured conductance across all 8 samples at all temperatures and pressures is 670 W/(m^{2}K) with a standard deviation of 275 W/(m^{2}K).

Since no pressure dependence is seen in these measurements, higher pressures might need to be investigated. Further, because the contact pressure at the jelly roll-case interface is unknown, and changes with the number of charge-discharge cycles that a battery goes through, a similar experimental approach needs to be used to measure the interfacial conductance at the actual contact pressure by using a cross-section of an Li-ion battery surrounded by reference layers, in an *in situ* configuration. This work is discussed in Chapter 3.

CHAPTER 3. CYLINDRICAL BATTERY CHARACTERIZATION

Chapter 3 derives from a conference publication draft. A. Gaitonde, A. Nimmagadda, A. Marconnet: Experimental Characterization of Thermal Conductance across the Separator-Shell Interface in Dry Cylindrical Lithium Ion Batteries, in *IEEE The Intersociety Conference on Thermal and Thermomechanical Phenomena in Electronic Systems (ITHERM)*, 2017.

3.1 Introduction

With the advent of hybrid vehicles and their increasing popularity, Lithium ion batteries have gathered prominence in the recent years. Though they were used in small scale devices from a long time, their applications in the automotive industry have caught the attention of many researchers. Even though Lithium ion batteries are sought after due to their high energy densities when compared to other available batteries [26], their usage is limited by the high heat generation associated with continuous operation. Past work has mainly focused on determining the electrochemical properties of these batteries. But the safety concerns related to the batteries have turned the attentions to the thermal aspects of the battery operation [4;27–32]. Considerable work in both experimental and computational domain has been done to determine this heat generation rates and internal temperatures within a battery using techniques such as hot plate technique and xenon flash technology [33;34]. In order to better understand the thermal characteristics associated with the battery operation, researchers have tried to estimate various properties of the battery such as specific heat and thermal conductivity. Some have also reported the thermal conductivity of individual battery components such as cathode and anode [35;36]. Additional studies have been conducted to estimate the thermal runway of the batteries that leads to

explosion [37]. Recent studies aimed at determining the thermal conductivity values in both both in plane and cross plane directions for batteries of different compositions [7; 38]. Though the batteries are anisotropic in nature heat transfer across the battery layers in the perpendicular direction is the determining factor in removing heat from the outside of the cylindrical battery cell.

Among the many thermal properties associated with a lithium ion battery, the interfacial thermal resistances, or in other words, the thermal conductance between the plastic separator (the outermost layer in the battery jelly roll) and the steel shell of the battery is a property of significant interest, since the heat transfer across this interface to the surroundings is a key factor in determining thermal runway and to ensure safety of the charging and discharging processes of the battery, especially at high current rates. Knowing the thermal conductance will give a quantitative idea on the effectiveness of this heat transfer. In this chapter, the thermal conductance of 18650 cylindrical cells is evaluated in a radial configuration, by constructing a dry 18650 battery using the same electrodes that constitute a functional battery.

3.2 Experimental Methodology

The diameter of a cylindrical 18650 Lithium Ion battery is 18mm, and the height is 18650 (and hence the '18-65-0' nomenclature). The individual electrodes are only a few microns thick (around 100 to 150 μm, depending on the chemistry and type), while the porous plastic separator is about 25μm thick. At these length scales, it is challenging to spatially resolve temperature gradients across the stack in the radial direction with conventional thermal metrology tools (e.g thermocouples, RTDs, etc.). Here, to measure thermal conductivity and thermal conductance across the battery stack, an infrared microscope is used. In cylindrical batteries, heat transport is dominated by radial heat transfer, and the gradient along the vertical or axial direction is negligible, due to two factors: nearly uniform heat generation happening throughout

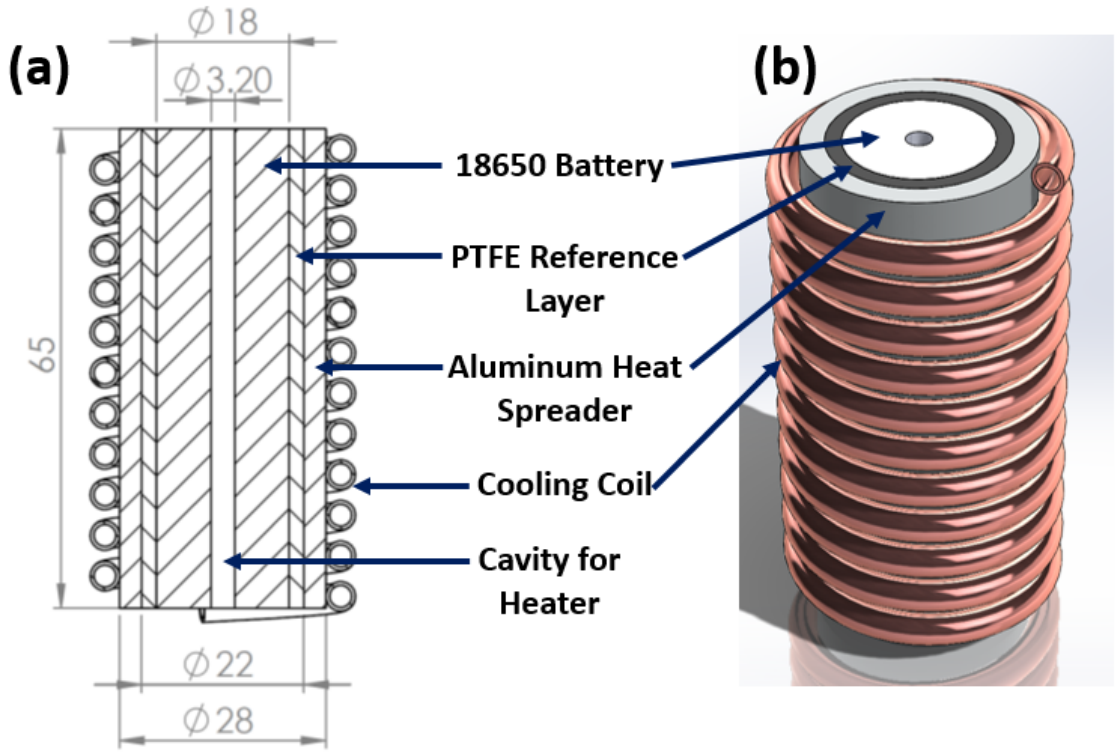

Figure 3.1. (a) A cross-section and (b) 3D model of the *insitu* test rig. The axial cavity in the center of the constructed 18650 battery holds a cartridge heater. The battery is enclosed inside a sleeve of PTFE (Teflon), which is used as a reference material to quantify heat flow through the battery. The PTFE sleeve is surrounded by an aluminum heat spreading sleeve, which is in contact with a coil heat exchanger. All dimensions shown in (a) are in mm.

the core of the battery [16] and the large aspect ratio(L/d 3.6). The design and working of a cylindrical battery test rig is discussed in the following sections.

3.2.1 Design of a Cylindrical Battery Test Rig

To measure the thermal conductivity of the battery and interfacial thermal conductance across the separator-case interface, a temperature gradient needs to be established in the radial direction. To achieve this, a dry battery is constructed with a

is a cavity for insertion of a 60 Watt miniature cartridge heater (Firerod Heaters from Watlow) in the center of the cell. To measure the heat rate in the system, the battery is enclosed in a cylindrical sleeve of 'reference' material. The temperature gradient in the reference material is also recorded by the infrared microscope. In this work, high temperature polytetrafluroethylene (PTFE), commonly and commercially known and available as Teflon [39], is used as the reference material. The thermal conductivity of this material (k_{ref}) is known, and is verified using a certified reference material for thermal conductivity from the National Institute of Standards and Testing [40]. By measuring the temperature gradient in the reference material, the heat flow rate through the system is given by,

$$q_r = \frac{\Delta T}{\frac{log(\frac{r_o}{r_i})}{2\pi k_{ref}}} = \frac{T_{ro} - T_{ri}}{\frac{log(\frac{r_o}{r_i})}{2\pi k_{ref}}} \tag{3.1}$$

where, T_{ro} and T_{ri} are the temperatures of the extreme ends of the reference layer, corresponding to r_o and r_i, which are the outer and inner radii of the reference sleeve respectively.

While the cartridge heater generates heat in the core of the battery, on the outer surface of the battery, an active cooling method is employed to conduct the heat away, to create a temperature difference across the battery stack. Thus, the outer surface of the reference sleeve is enclosed by a cylindrical Aluminum heat spreading sleeve, which has a winding of copper tubes on its outer perimeter, that act as a heat exchanger. The $1/8^{th}$ inch ID copper tubes are connected to heat spreading sleeve using thermal cement. The ends of the copper tube are connected to a constant temperature heat transfer fluid. The temperature of the fluid is set to any desired value between -20°C and +200°C, and its flow rate can also be controlled to achieve any desired heat removal rate. It is important to note that the battery, reference sleeve, and the aluminum heat spreading sleeve are concentric, with transition fits at their mating surfaces. Before assembly, the interfaces between these are smeared

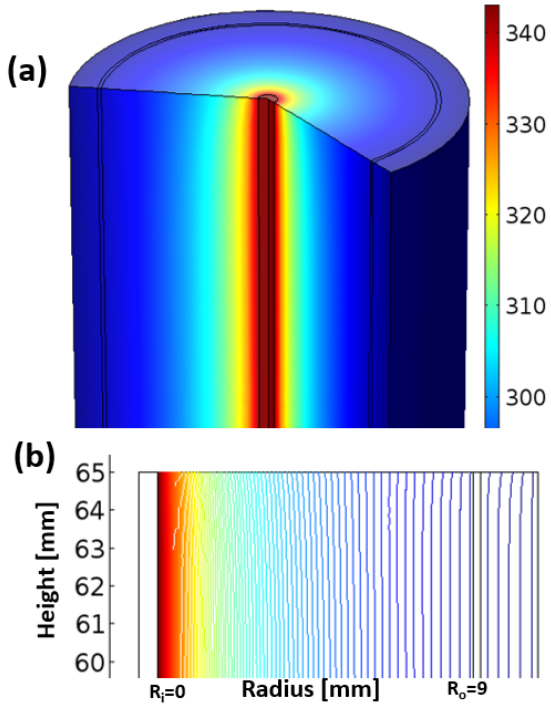

Figure 3.2. (a) Cross-sectional view of the temperature distribution in a battery structure when heat is generated inside the central cavity, as predicted by the simulations conducted in COMSOL, and (b) the corresponding isotherms near the top surface of the battery where the infrared images are recorded. The isotherms are reasonably parallel, which signifies that heat transport is approximately 1D in the radial direction, and that convection losses are insignificant.

with a thermal interface material (TIM) to improve thermal conductance across the interfaces. Figure 3.1 shows a cross section of the test rig, along with a 3D view of the design.

3.2.2 Verification of Design Accuracy

Before machining and manufacturing the test rig, the system is modeled as an axisymmetric case in a commercial finite element package, COMSOL, to verify the performance and accuracy. The crucial parameters verified with the model are the heat flow paths, convection losses, and the effects of heat flow in the axial direction.

To simulate the experiment, a constant temperature boundary condition is defined at the heater cavity, and a similar boundary condition is applied at the outer cold surface of the Aluminum heat spreader. Since the experiments are conducted in air, the heat transfer coefficient from the top surface is varied as a parameter from $10\,\mathrm{W/(m^2\,K)}$ to $50\,\mathrm{W/(m^2\,K)}$, to check if convection losses from the exposed surfaces are significant. Figure 3.2(a) shows a sectional view of the results of the simulation, at steady state. Figure 3.2(b) shows the corresponding isotherms near the top surface of the battery, where the infrared measurements are recorded, and they are found to be reasonably parallel, for the range of convection losses investigated. This is expected, since the thermal resistance to convection is about 20 times higher than the thermal resistance to conduction. The thermal resistances are given by

$$R_{th,cond} = \frac{log(\frac{r_o}{r_i})}{2\pi L k_{battery}} \; and \quad R_{th,conv} = \frac{1}{hA} \tag{3.2}$$

where, $R_{th,cond}$ and $R_{th,conv}$ are the thermal resistances to conduction and convection, respectively, $k_{battery}$ is the predicted thermal conductivity of the battery stack, and h and A are the heat transfer coefficient and surface area exposed to convection, respectively. For a predicted effective thermal conductivity of the battery stack of 0.3 W/m/K, and a heat transfer coefficient of 15 $\mathrm{W/m^2K}$, the thermal resistances to conduction and convection are 13.3 K/W and 272.2 K/W respectively.

3.2.3 Manufacturing the Test Rig

Figure 3.3 (a) shows the experimental setup with (b) the test rig embedded into a ceramic block for insulation and support. The battery jellyroll is constructed using electrodes, separator, and the 18650 metallic shells purchased from MTI Corporation, Richmond, CA. The battery cathode is a double side coated Aluminum foil with $LiFePO_4$, while the anode is a single side coated copper foil with CMS graphite. The aluminum and copper act as current collectors, whereas the coatings are the active battery materials. The plastic porous separator is 25µm thick, and is made

out of polypropylene, commercially known as Celgard. Long strips are cut to size, and then rolled along until the diameter of the roll becomes 18mm, after which it is pushed into the empty 18650 shell, as shown in Figure 3.3(c). The reference sleeve is machined from a block of black PTFE, while the heat spreading Aluminum sleeve is machined from an oversize Aluminum rod. Both these operations are done on a lathe. After the rig is assembled, it is placed in a ceramic block which serves two purposed, (1) it acts an an insulator, keeping the heat exchanger from losing heat to the ambient, and (2) it keeps the rig aligned vertically under the microscope. Swagelok compression fittings connect the ends of the coil heat exchanger to the constant temperature fluid bath, and ensure a leak proof and removable connection. Two fine gauge T-type thermocouples are attached near the heater cavity and on the Aluminum sleeve, to record the maximum hot side and cold side temperatures in the system. These readings are recorded by an NI-9213 data acquisition system, and are secondary measurements for reference purposes only. The primary temperate measurements that are used to characterize the thermal conductivity and thermal conductances across the battery are recorded by the infrared microscope.

3.3 Results and Discussion

3.3.1 Data Acquisition and Analysis

For calibrating the emissivity, *i.e.*, the battery is initially heated to a known uniform temperature (the reference temperature), and the radiance is measured by the infrared (IR) Microscopes sensor. Since the reference temperature is known, by comparing this radiance to that of a black-body a the same temperature, the emissivity at each pixel is calculated for the sample, which is then used for calculating other unknown temperatures when a temperature gradient is created. Figure 3.4(a) shows a 2-dimensional temperature map, as measured by the IR microscope, with $(1024)^2$ temperature data points across a 9 mm^2 field of view. This temperature map is then imported into MATLAB, and different areas of the sample (reference region,

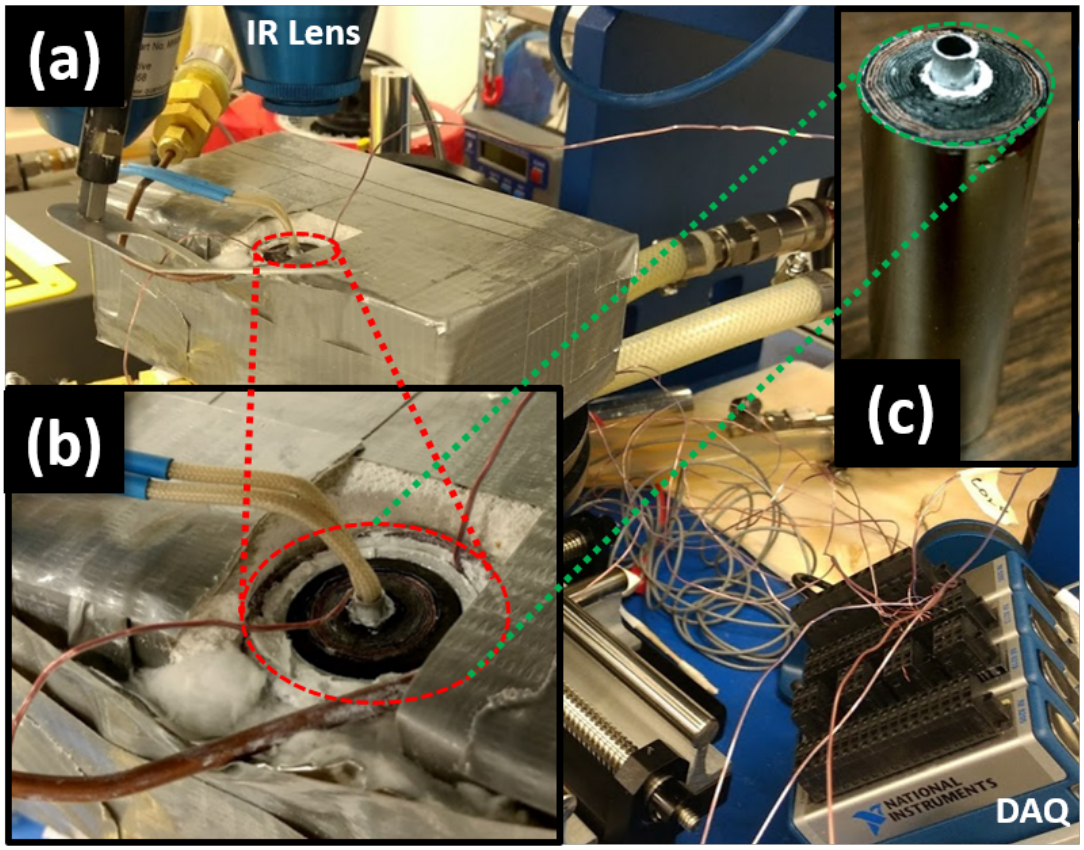

Figure 3.3. (a) The experimental setup consisting of the manufactured test rig housed in a ceramic insulator brick, with (b) heater leads running out from the top along with fine gauge thermocouple wires which are connected to a voltage regulator (to control heat flux), and to a National Instruments DAQ respectively. Note that the thermocouple measurements are to measure the extreme system temperatures, *i.e.* the hot side and the cold side temperature, for general reference only. The primary measurements are done by the infrared microscope, whose 1x objective lens is marked in the picture. (c) shows the constructed 18650 dry battery which is housed in the *in situ* measurement rig.

battery region, heater region) are identified by custom image processing scripts. Since the heat transfer is radial, the temperature along any given arc inside the battery are constant, and are averaged to transform the 2-dimensional temperature map to an

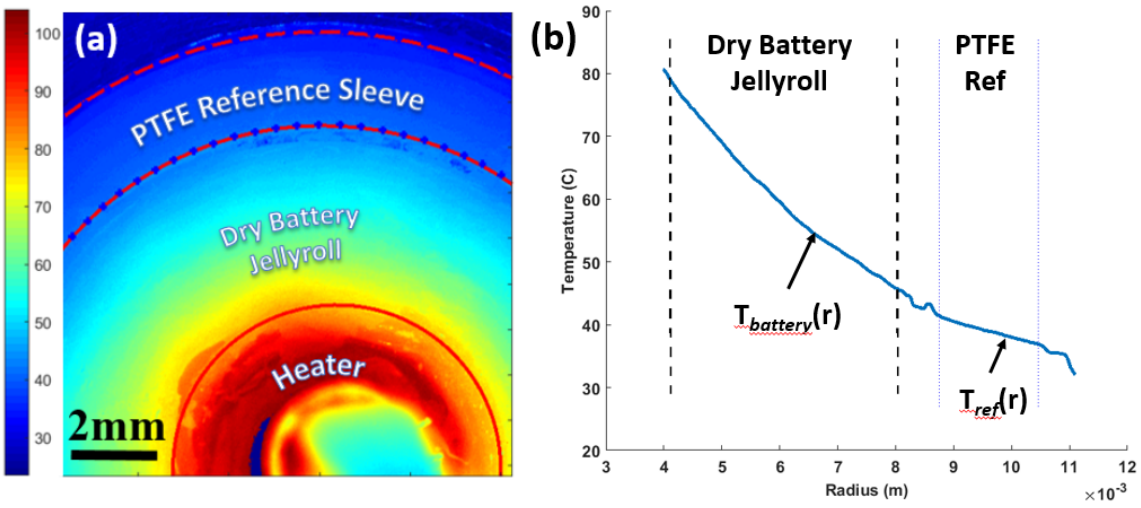

Figure 3.4. (a) A 2D temperature map of the top surface of a dry 18650 battery. Heat flows from the axial heater, across the battery jellyroll and the reference layer to the heat sink. (b) The corresponding arc averaged 1D temperature profile. The temperature gradient in the reference region is used to calculate the heat rate flowing across the battery.

averaged 1-dimensional temperature map, as shown in Figure 3.4(b). For 1D radial heat transport, a logarithmic temperature decay is expected and observed.

3.3.2 Heat Rate and Thermal Conductivity

The heat rate flowing across the battery-reference structure is given by

$$q_r = \frac{(T_o - T_i)_{ref}}{\frac{log(\frac{r_o}{r_i})_{ref}}{2\pi L k_{ref}}} = \frac{(T_o - T_i)_{battery}}{\frac{log(\frac{r_o}{r_i})_{battery}}{2\pi L k_{battery}}} \tag{3.3}$$

where $(T_o - T_i)$ is the temperature drop in the reference region, r_o, r_i, and k are the outer and inner radii, and the thermal conductivity respectively. The subscripts 'ref' and 'battery' refer to the reference region and the battery (sample) region respectively.

The effective thermal conductivity of the battery jellyroll, is then calculated as,

$$k_{battery} = \frac{q_r}{2\pi L} \frac{log(\frac{r_o}{r_i})}{T_o - T_{i\,battery}}. \tag{3.4}$$

From Equation (3.4), the slope of the variation of the heat rate measured in the reference q_r with $\frac{2\pi L(T_o - T_i)_{battery}}{log(\frac{r_o}{r_i})_{battery}}$ gives the fitted thermal conductivity, as shown in Figure 3.5.

3.4 Conclusions

To measure the thermal conductivity of cylindrical 18650 cells, an *in situ* test rig (based on a radial version of the conventional reference bar method) has been designed, validated using COMSOL, manufactured, and tested with a dry battery cell. A dry 18650 battery has been constructed using electrodes from MTI Corp. The effective fitted thermal conductivity of a dry 18650 battery, in a radial configuration, is measured to be 0.32 W/m/K, and is found to be 0.05 W/m/K higher than that measured in a linear configuration (see Section 2.4.3). It should be noted that this value of thermal conductivity incorporates effects of the active electrode materials, metallic current collectors, and thermal interface resistances within the stack.

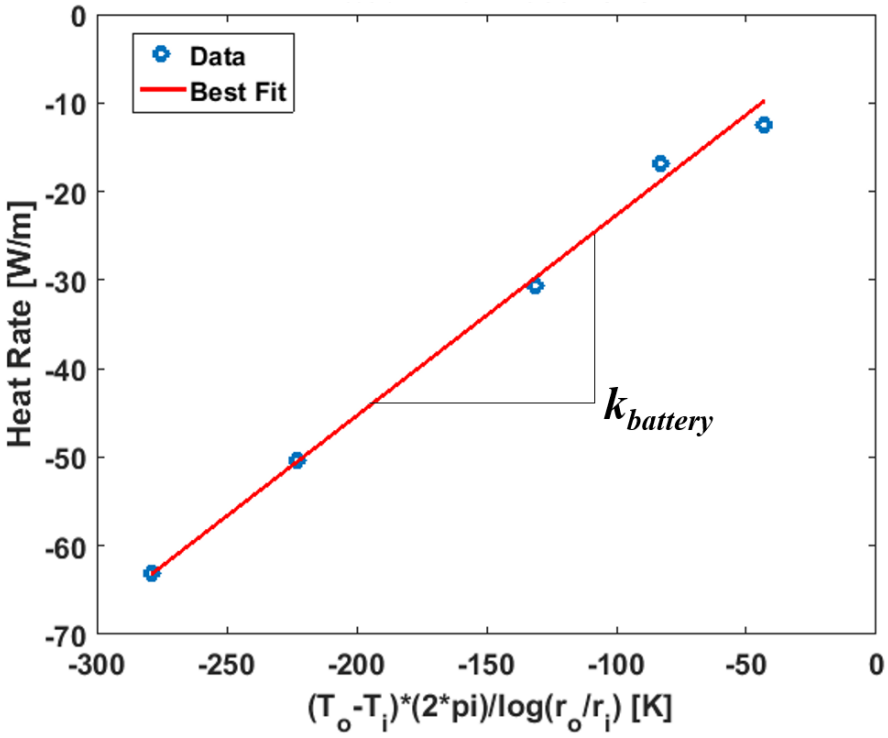

Figure 3.5. Fitted thermal conductivity of the battery stack, as a function of the heat rate. The measured value of $k_{battery}$ is 0.23 W/m/K.

3.4.1 Future Work

This work measures the effective thermal conductivity of dry batteries, in the absence of an electrolyte. In an active battery, it is predicted that the thermal conductivity will be higher, due to the presence of the electrolyte, which might provide better surface to surface contact across the stack of electrodes. To this effect, a inert gas chamber is being designed, which will be filled with Argon. The chamber will fit around the cylindrical battery test rig, with a Calcium Fluoride (CaF_2) window over the top surface, through which infrared measurements will be recorded. Instead of a dry battery, a commercial 18650 battery cut open at the top and bottom, as shown in Figure 2.9(a), will be inserted in the test rig, without harvesting the jellyroll. This

will enable thermal conductivity measurements of an actual 18650 battery, with the electrolyte, without having to harvest the electrodes and at actual contact pressure.

CHAPTER 4. CHARACTERIZING THERMAL TRANSPORT IN SHEARED GRANULAR BEDS

4.1 Introduction and Motivation

Controlling heat conduction in disordered granular systems is critical to the design of functional materials for energy conversion and storage applications such as granular-like electrodes in lithium ion battery electrodes, suspensions in flow batteries, and packed nanoparticles in thermoelectric devices [41; 42]. The microstructure, grain size and shape, and contact topology of packed granular materials govern their effective thermal properties, such as the effective thermal conductivity and thermal contact resistance. External mechanical perturbations such as compression or shearing can induce microstructural rearrangements. Often, such stresses occur during material manufacturing or processing, as well as during field operation, and a detailed understanding of the microstructural response to stress also allows for the possibility of developing application-specific tailored composites.

Specifically, in this work, the effects of grain shape, grain size, and external stress on the effective thermal conductivity of packed granular materials are examined. In particular, the thermal images from IR microscopy highlight the dominant pathways for heat conduction in granular materials with large microstructural heterogeneity. Previous simulation work has identified the role of contact topology in thermal conduction through granular materials [43]. The efficacy of effective medium approximations in the prediction of effective thermal conductivity of dense packings of tetrahedra was explained on the basis of a lack of face-to-face tetrahedral contacts. Additionally, past experiment [44] and simulation [45] work has also shown that the aspect ratio of hexagonal bismuth telluride nanoplatelets, that are compacted into thermoelectric

pellets, plays a dominant role in effective thermal conduction by impacting the net scattering rate of phonons at grain boundaries.

Lithium ion battery electrodes are composite materials, consisting of current collectors, generally made of Aluminum and Copper, with surface coatings which act as receptors and release agents of Lithium ions. As an example, the anode structure consists of a Copper film, coated with graphite powder. During manufacturing, a slurry or a paste of graphite powder in a binding agent is applied on the Copper film, and the thickness is reduced by calendering [41; 42; 46; 47], and during this process shear stresses are induced in the thin layer of graphite, by the two cylindrical rollers in the calendaring operation. Past work has also shown that increased diffusion rates are achieved through reducing the diffusion length, by controlling the electrode dimensions [31]. In depth understanding of the changes in thermal conductivity caused by the shearing operation could also help in better designed batteries from a thermal standpoint, since many Lithium ion battery accidents have recently been reported [48–50].

This study aims to directly identify the mechanisms for the changes in effective thermal conductivity in disordered granular packings. The two-dimensional temperature maps illustrate how heat conduction pathways change as a result of external mechanical stresses induced by Taylor-Couette flows. An empirical understanding of the correlation between microstructure, and the effect of shearing on the effective thermal conductivity of granular materials. A cylindrical Taylor-Couette cell is designed, modeled and fabricated, for the purpose of investigating thermal conduction pathways in packed granular beds and the effect of shear on these pathways. An infrared (IR) microscope with a temperature resolution with a spatial resolution of 1.8 µm of 0.1 K aids in the direct observation of heat conduction through the particles in packed beds of granular matter. Controlling and predicting optimum microstructure of packed granular media for tailored properties is crucial.

4.2 Experimental Methodology

To measure the effect of mechanical shear on heat transport, *viz.* effective thermal conductivity of packed granular media, a test rig, the 'Taylor Couette Cell' has been designed, modeled, and fabricated. Thermal measurements are performed using infrared imaging with high spatial resolution. The emissivity of the surface is calibrated at every pixel is by heating the system to a known temperature, and then taking a 'Reference Map', where the radiance emitted by the device under test is measured and is compared with the radiance emitted by a black body at the same temperature. The test rig has the ability to shear a packed bed of granular material by sandwiching granular media between two concentric cylinders, and then rotating the cylinders respective to each other. The concentric cylinders are open at one end, which serves two purposes: (a) it provides an opening through which the granular material can be filled into the cavity until it is completely filled, and (b) the temperature profiles at this surface are mapped using the infrared microscope. The inner cylinder is heated and the outer cylinder is cooled, thereby creating a temperature gradient across the sample granular material which is sandwiched in between the two cylinders. Temperature measurements are taken before and after shearing, and the difference in the thermal conductivity is due to shearing. The heat rate flowing through the system is measured by incorporating reference materials of known thermal conductivity. By measuring the temperature drop across the reference materials, the heat rate is calculated. Figure 4.1 shows a graphical representation of the first version of the test rig, with the different parts labeled.

4.2.1 Overview of Design

The 'Taylor Couette' cell, generally referred to as the 'Couette Cell', is primarily a set of concentric cylinders, with an annular cavity between them. The inner cylinder rotates, while the outer cylinder is held stationary. The annular cavity, which is flanked by the outer surface of the inner cylinder and the inner surface of the outer

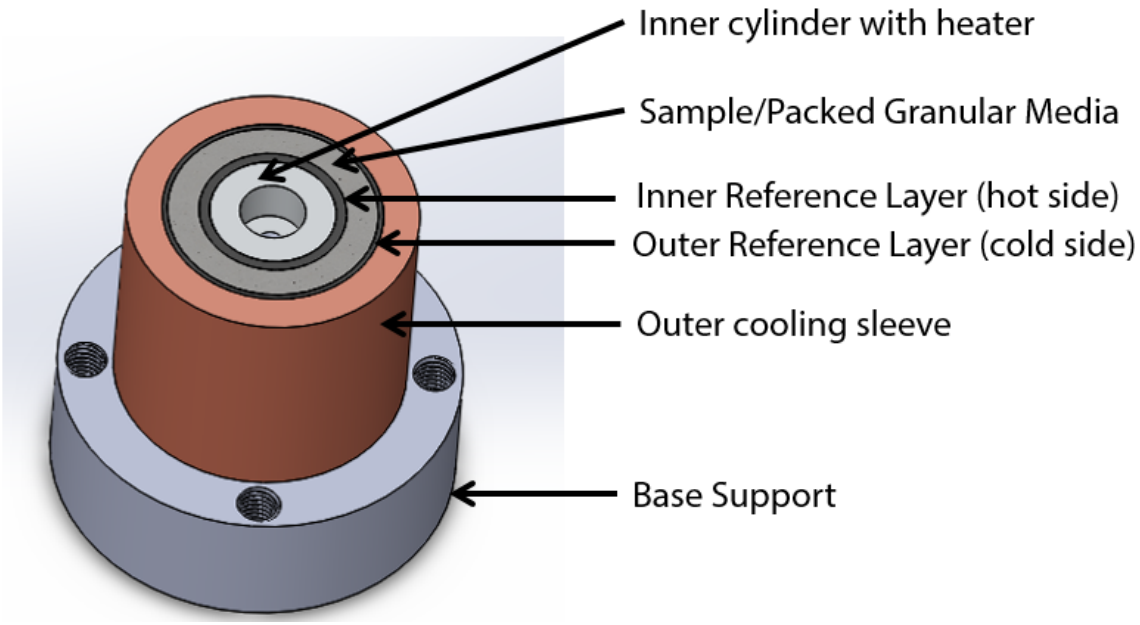

Figure 4.1. A 3D CAD model of the first version of the Couette Cell. The inner cylinder, which houses a cartridge heater, rotates, while the outer cylinder with a built in helical heat exchanger is held stationary

cylinder, is filled with granular media, and is sheared by the rotation of the inner cylinder. The inner cylinder is a thick walled aluminum tube, where the 1/4" central cavity allows for a stainless steel shaft to be press fitted with an FN1 Force Fit (Interference Fit), and at the other end (top end), the cavity is slightly enlarged to have a clearance fit with a 1/4" 60 W Watlow Firerod cartridge heater. The heater, when connected to power, expands slightly, making contact with the Aluminum cylinder. The shaft of the inner cylinder is connected to a DC motor via a flexible shaft coupling, which allows for a very slight misalignment between the shaft of the motor, and that of the inner cylinder.

In the outer cylinder, a helical coil heat exchanger is cut in a thick walled aluminum cylinder. Another thin walled aluminum sleeve is press fitted concentric to

this cylinder's outer surface, effectively creating a heat exchanger. The top and the bottom are then welded to prevent any leaks of the heat transfer fluid.

Both the inner and outer cylinders are lined with layers of high temperature polytetrafluroethylene (PTFE). The thermal conductivity of this reference material is known, and is verified with a certified standard reference material from NIST. PTFE is chosen because it is easy to machine, widely available commercially, and it is cheap compared to certified reference materials. These linings are thin walled cylinders, press fit on the outside surface of the inner cylinder (call out 3 in Figure 4.2), and the inside surface of the outer cylinder (call out 6 in Figure 4.2). When a temperature gradient is applied, these reference layers are used to quantify the heat rate in the radial direction.

This entire assembly is supported by an external support structure, which keeps the Couette Cell vertically below the lens of the IR Microscope.

4.3 Data Acquisition and Analysis

The recorded thermal images are in the form of 2 dimensional matrices, with $(1024)^2$ temperature data points. To accommodate the dimensions of the Couette Cell, a 1x objective lens is used, which results in a part (121 mm^2) of the reference-sample-reference being imaged. This temperature map is imported into MATLAB for post processing, where the user selects the inner and outer circumferences of the reference layers, by selecting three points on each circumference. Using an algorithm to fit a three point arc in the selected points, the coordinates of the center of the circle that the arc is a section of is calculated. This procedure is repeated for all edges of the two reference layers, and these fitted arcs are shown as red circles in Figure 4.3. While the centers of these four circles is calculated independently of each other, the coordinates of their centers are averaged to compute a common center. The four different radii are then picked again, to refine the accuracy of the geometric arcs superimposed on the temperature image corresponding to the physical dimen-

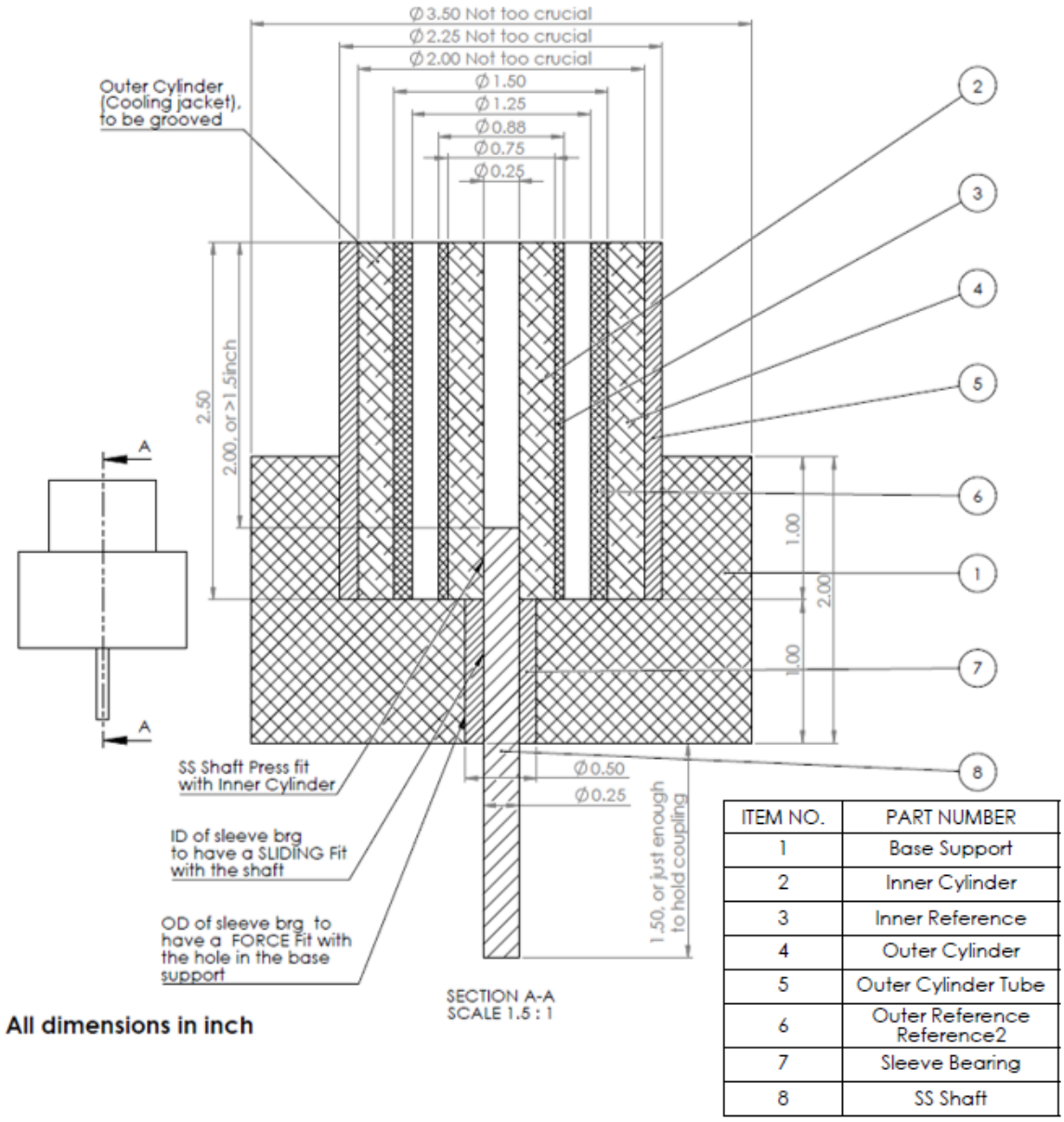

ITEM NO.	PART NUMBER
1	Base Support
2	Inner Cylinder
3	Inner Reference
4	Outer Cylinder
5	Outer Cylinder Tube
6	Outer Reference Reference2
7	Sleeve Bearing
8	SS Shaft

Figure 4.2. A cross sectional view of the assembly of the first version of the Couette Cell with a shorter base support, with all parts enlisted, and the type of fits of crucial components.

sions. These are shown as bolded blue points on the red arcs in Figure 4.3, and the corresponding radii with the common center are denoted by R_1 through R_4.

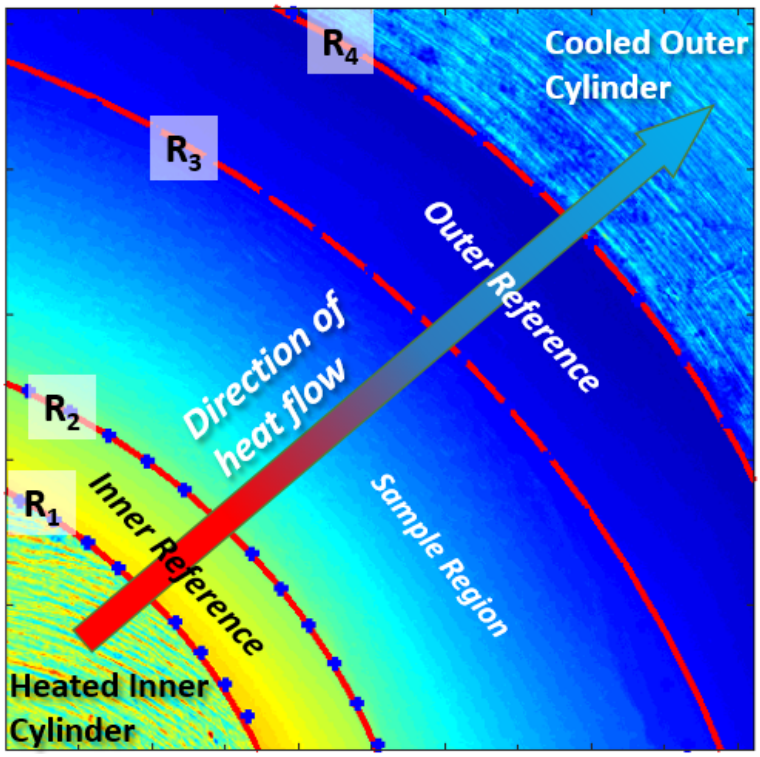

Figure 4.3. Different regions such as the inner reference, sample, outer reference, are marked on the 2D temperature map by the red arcs. These arcs are fitted after three points are selected visually for each circular edge of interest (inner reference inner and outer periphery, outer reference inner and outer periphery, *etc.*), and an algorithm in MATLAB fits a three point arc in the selected data points. These red arcs do not have a common center. All centers are subsequently averaged, and the bolded blue dots represent corresponding geometric arcs with a common center, which corresponds to the actual central axis of the Couette Cell.

The area between the outer circumference of the inner reference layer, and the inner circumference of the outer reference layer is the sample region. Since heat transport is radial, temperatures along any given radius should be equal, and the temperatures are averaged by dividing the region between the inner circumference of the inner reference (R_1) and the outer circumference of the outer reference (R_4) into radial wedges of finite width. The script marches through all wedges, averaging all

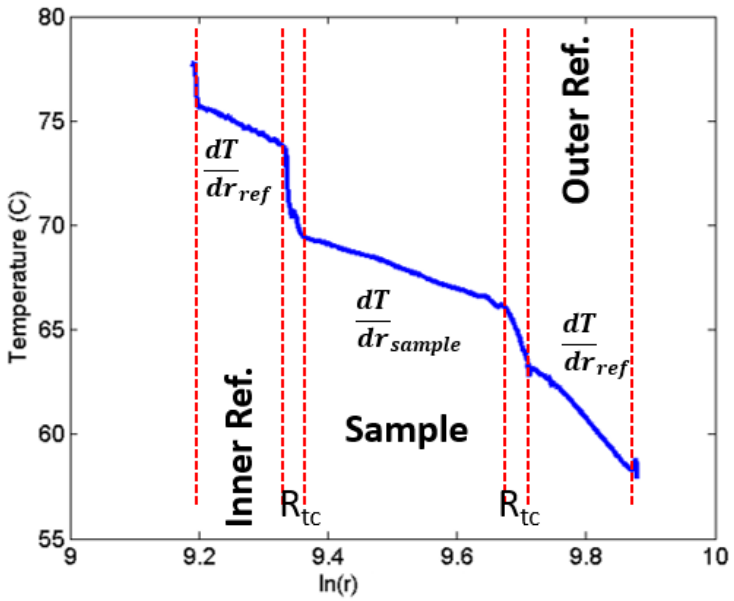

Figure 4.4. A representative arc averaged 1D temperature profile corresponding to the 2D temperature map shown in Figure 4.3. R_{tc} is the thermal contact resistance between the reference layers and in the sample layer. Here, the sample region is a Teflon cylinder machined to the sample size. Note that the abscissa is log(r), which makes the temperature decay linear, and not logarithmic.

temperatures that fall within a particular wedge. Figure 4.5 shows a representative 2D temperature map averaged to a 1D temperature profile.

4.4 Validation with Reference Materials

Before the rig is used with granular media, measurements are performed with known reference materials. The inner and outer reference layers were machined out of blocks of white Teflon^{TM} and hence, as a benchmark, a sample of white Teflon^{TM} has been machined to the same dimensions as the cavity between the two cylinders, to measure the thermal conductivity of this known material. This sample is then inserted in the cavity, and a temperature gradient is created across the sample. Since the heat rate across the reference-sample-reference structure remains constant, by

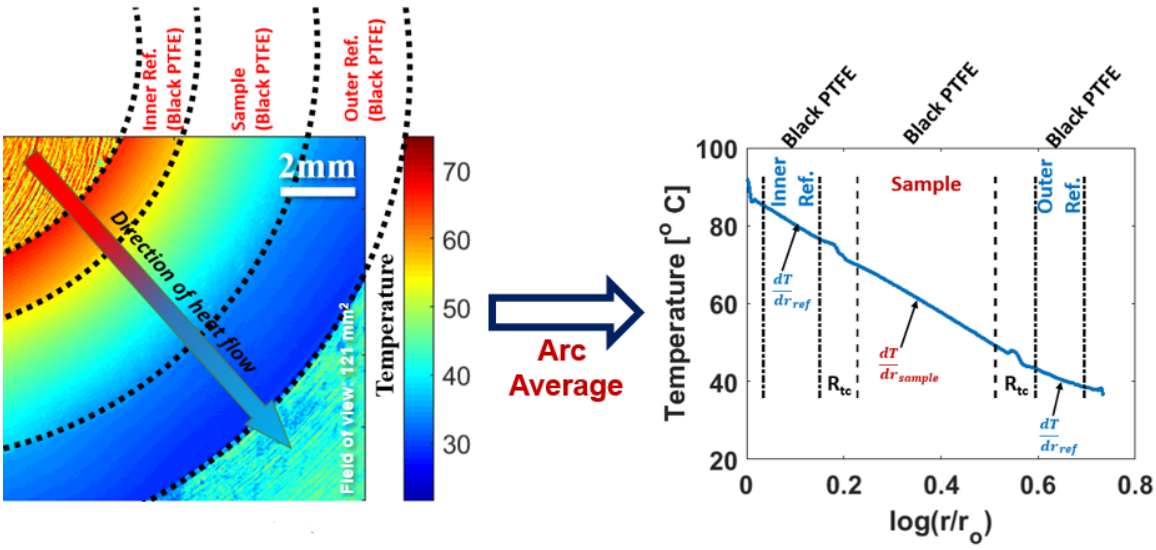

Figure 4.5. A 2D temperature map converted to an arc averaged 1D temperature profile.

measuring the temperature gradient in the sample and reference regions, and the thermal conductivity of the sample is calculated using

$$k_{sample} = k_{ref} \frac{log(\frac{r_o}{r_i})_{sample}}{log(\frac{r_o}{r_i})_{ref}} \frac{\Delta T_{ref}}{\Delta T_{sample}} \tag{4.1}$$

where k_{ref} and k_{sample} are the thermal conductivities of the the reference material, and the sample material, respectively, r_o and r_i represent the outer and inner radii of the two cylindrical reference layers and the sample.

If this measured thermal conductivity is equal to that of the reference material, it can be concluded that the test rig functions as expected. Experiments with black Teflon (reference material) used as a specimen yield a measured (calculated) thermal conductivity of 0.29 W/m/K, which is within 3% of its actual thermal conductivity. These experiments were performed using a heated enclosure (see Section 4.4.2) to address some experimental challenges, as discussed in Section 4.4.1.

4.4.1 Challenges

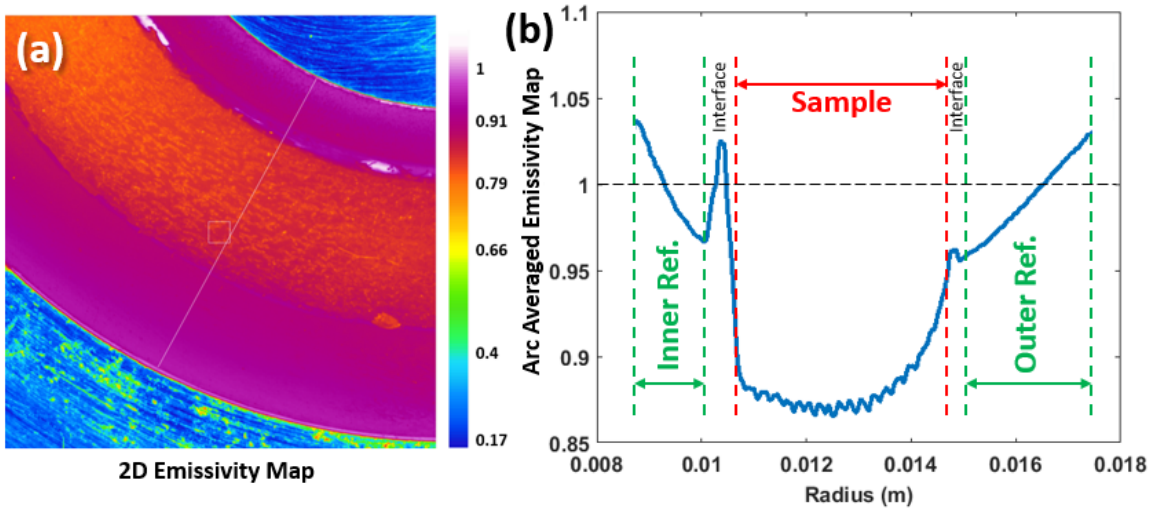

Figure 4.6. (a) A 2 dimensional emissivity map of the reference-sample-reference structure, where both the reference layers and the sample is the same material - black Teflon. The Aluminum (inner and outer cylinder) areas show low emissivity

Figure 4.6(a) shows the spatial variation of emissivity of the reference-sample-reference structure as measured by the IR microscope, where both the reference material and the sample material is the same - black Teflon. The 'Reference Mapping' is the first step in the thermal imaging process, where emissivity is calculated for each pixel by heating the entire sample to a known temperature. Although the experiment is conducted in the presence of air, the thermal resistance to convection is two orders of magnitude higher than that to conduction, and hence it was expected that convection losses would not be significant. As an example, the thermal resistance to conduction is calculated to be 3.1 K/W and that to convection is 167.02 K/W in the black Teflon sample, which is given by

$$R_{th,cond} = \frac{log(\frac{R_3}{R_2})}{2\pi L k_{teflon}}; \quad R_{th,conv} = \frac{1}{hA} \tag{4.2}$$

where R_3 and R_2 are the outer and inner radii of the sample, L is the height of the sample across which heat transfer occurs, k_{teflon} is the thermal conductivity of black Teflon, 'h' is the predicted heat transfer coefficient, and 'A' is the top surface area of the sample that is exposed to convection.

Figure 4.6(b) shows the arc averaged emissivity along the radial direction. Note the low emissivity in the sample region, and the negative and positive slope in the inner and outer reference respectively, which signifies convection losses from the top surface.

4.4.2 Heated Box with Calcium Fluoride Window

The ambient air temperature where the experiments are conducted is 19 °C and, one way to verify if the low emissivity in the sample region is caused by cooling of the central portion of the sample due to convection losses is to heat the air around the rig to the same temperature as the top surface temperature. This is done by enclosing the Couette Cell in a temporary enclosure made of Acrylic. The heater leads and thermocouple leads are fed through small drilled holes, when are sealed using duct tape after the wires are fed through. The top of the enclosure has a thick Acrylic lid, with a stepped hole to house a Calcium Fluoride (CaF_2) window, which transmits 95%of infrared radiation. The emissivity calibration is done after the addition of the (CaF_2) window, which accounts for the transmission losses through the window.

Figure 4.7 shows the Couette Cell enclosed in the temporary acrylic box, under the IR microscope during a measurement. The air inside the enclosure is heated to the top surface temperature using three 60 Watt cartridge heaters connected to a voltage transformer. The air temperature inside the enclosure is monitored by two T-type thermocouples connected to a NI-DAQ.

Figure 4.8(b) shows the improvement in the emissivity calibration (along the radius) when the enclosure is used and the internal air is heated to the top surface temperature of the Couette Cell.

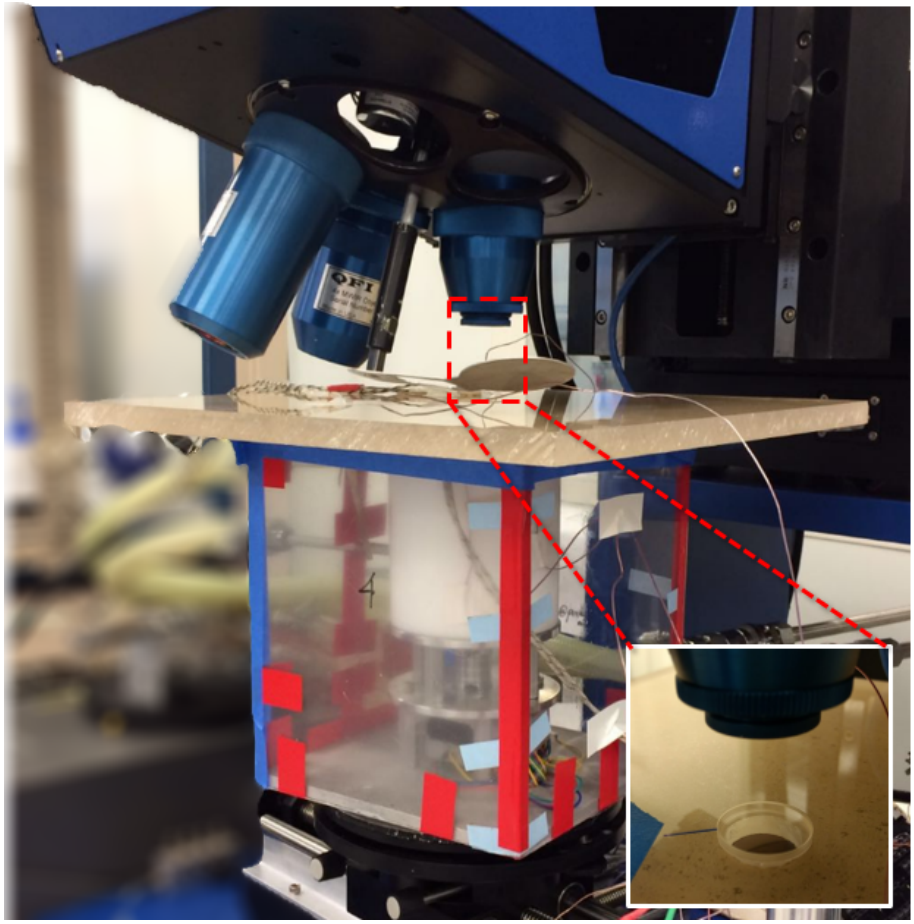

Figure 4.7. The Couette Cell enclosed in an acrylic box. This is an preliminary attempt of reducing convection losses at the top surface. The air inside the box is heated to match the surface temperature of the reference layers. A Calcium Fluoride window, which is transparent to infrared, is embedded in the Acrylic box lid through which the IR camera lens looks at the reference-sample-reference structure.

4.4.3 Vacuum with Calcium Fluoride Window

To reduce convection losses, another technique is to have a vacuum chamber to evacuate the air at the top imaging surface of the Couette Cell. Similar to the heated enclosure design (discussed in Section 4.4.2), imaging is done through a CaF_2 window embedded in the PTFE 'Cap', which is fitted on top of the Couette Cell. Figure 4.9 shows a cross sectional view of the PTFE cap that is designed to fit over the Couette

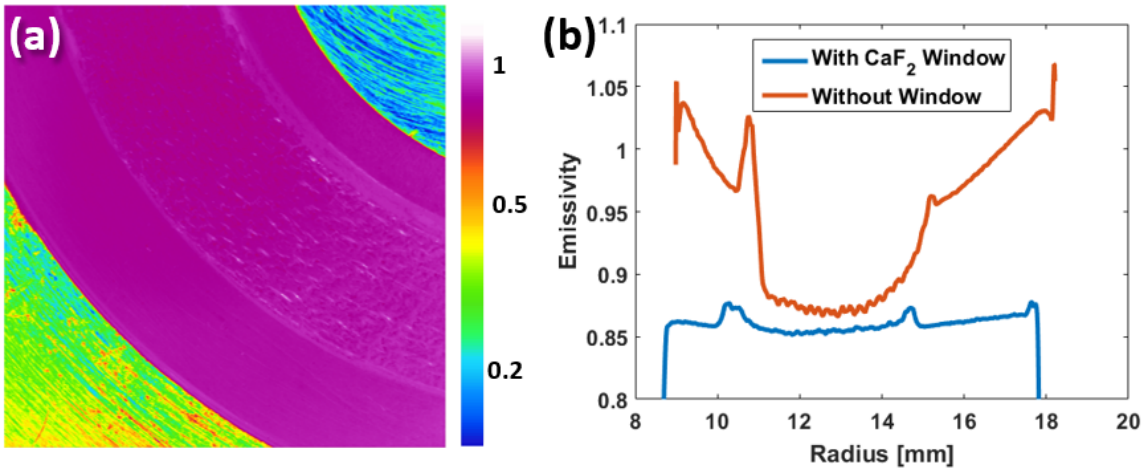

Figure 4.8. (a) A 2D emissivity map of the reference-sample-reference structure with black Teflon as the sample with the enclosure in place with heated air. The emissivity variation across the structure is significantly reduced as compared to the measurement without the enclosure and the CaF_2 window as shown in (b).

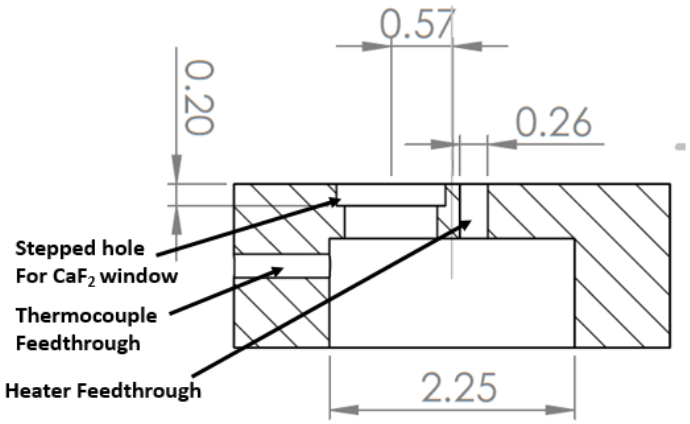

Figure 4.9. A cross sectional view of the vacuum cap that is fitted on top of the Couette Cell to evacuate the air from the top surface. Holes are drilled to provide feedthroughs for the thermocouple wires and heater leads.

Cell. At the mating surface of the cap and the Couette Cell, grooves are cut to seat O-rings to enable a leak proof fit.

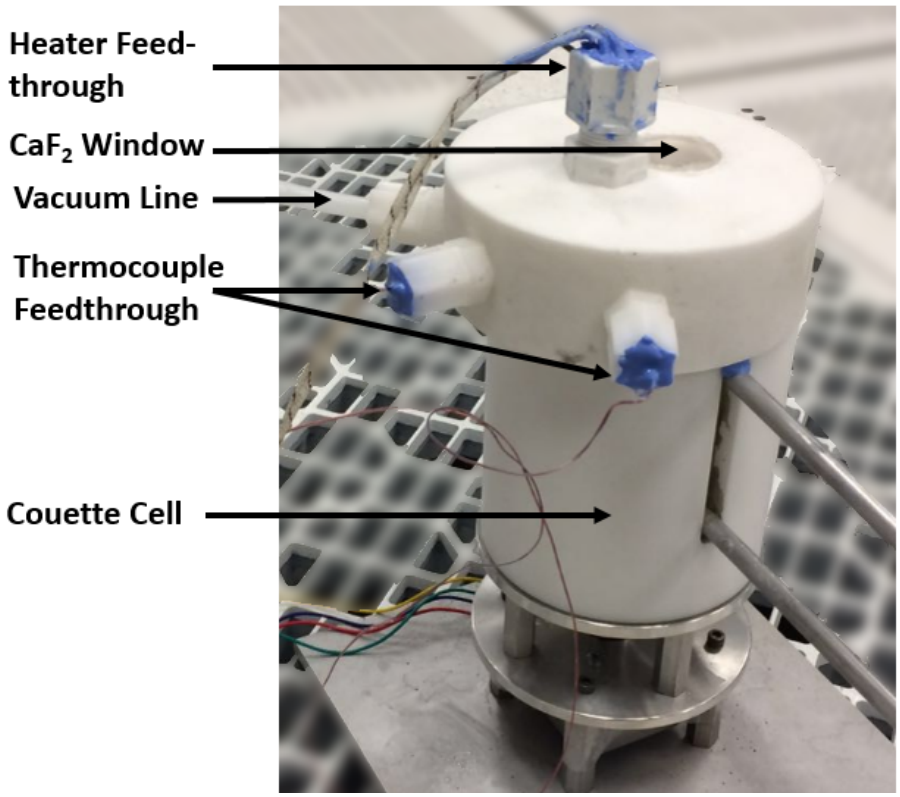

Figure 4.10. The Couette Cell is retrofitted with a PTFE cap using O-rings, and the air inside the cap and the top surface is evacuated by attaching a house vacuum line through the cap, in another attempt to reduce or convection lisses. Thermocouples and the heater leads are fed across the cap using compression fitting feedthroughs, which are sealed using an hard setting epoxy. A Calcium Fluoride window, which transmit in the infrared, is embedded in the cap, through which the IR lens focuses on the reference-sample-reference stack.

Figure 4.10 shows the Couette Cell with the PTFE vacuum chamber attached on top, with the thermocouple, heater feedthroughs and the CaF_2 window. Since this has been a retrofit design, a complete vacuum is not obtained and the leakage of air into the vacuum chamber is high. A more robust design is required to ensure a leak proof vacuum chamber.

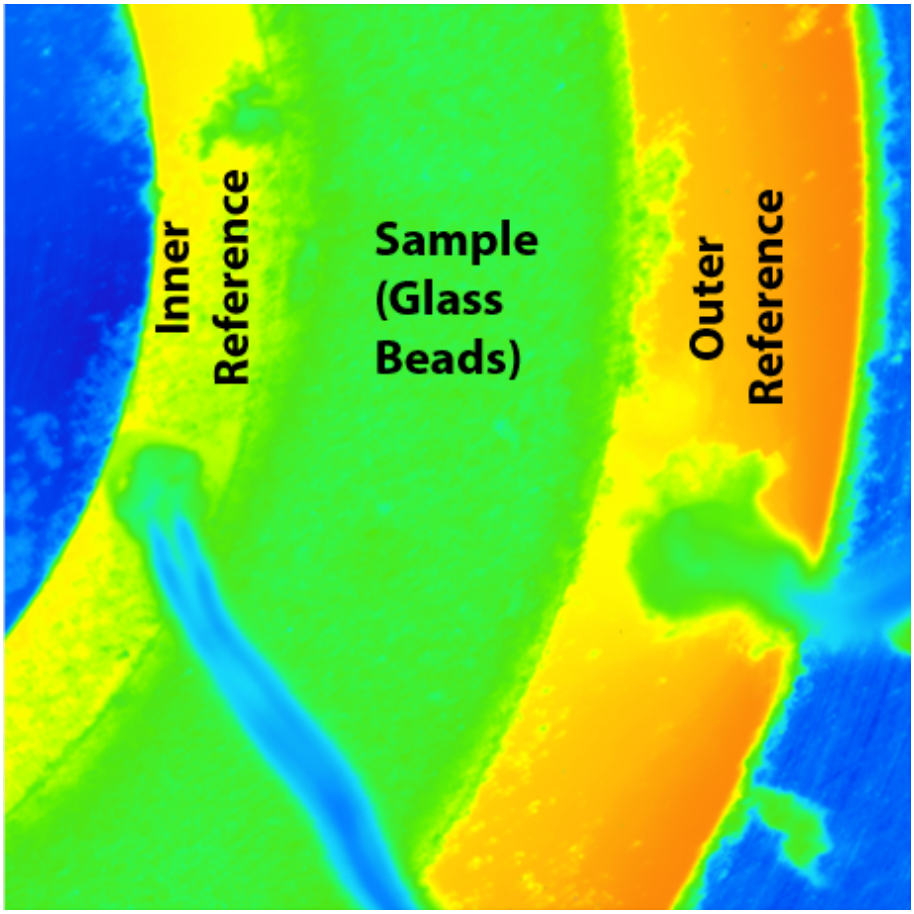

Figure 4.11. A representative emissivity map of the the Couette Cell filled with granular material (glass beads). Stray powder particles spilling onto the reference layers as experiments progress is a challenge. The wires that are visible are thermocouples connected to the reference layers.

4.5 Summary

A cylindrical Taylor-Couette has been designed and fabricated to apply shear stresses on packed granular media. This test rig is based on a radial equivalent of the conventional reference bar method [18], and is capable of simultaneously applying shear stresses and creating a temperature gradient across the packed bed of granular material. Although numerical simulations performed in COMSOL predict 1D heat transfer on the top surface of the Couette cell, significant convection losses are seen

in practice. To address this challenge, a heated enclosure is designed and built, with the internal air heated to the surface temperature. This reduces the convection losses significantly, yielding a flat emissivity map during the calibration phase of the IR microscopy. The test rig is validated using a standard known material, black Teflon, as the unknown sample, and its thermal conductivity is calculated, and is found to be within 3%of its known value . Experimental work with sheared powders are currently in progress.

CHAPTER 5. SUMMARY

5.1 Summary

The widespread popularity and manufacturing of consumer electronics has led to a exponential increase in the usage of lithium-ion (Li-ion) batteries, in applications such as cell phones, laptop computers, tablets, hover-boards, etc. Some of the advantages that Li-ion batteries offer are low discharge rates, low memory effects, high efficiency, low maintenance, etc. The United States Environmental Protection Agency (US-EPA) regulates the the emission standards in the US, and they are becoming more stringent every year. The NO_x emission standard has seen a 98%decrease in the past 25 years. This, coupled with incentives and subsidies from the government have fueled tremendous research, advancements and manufacturing of hybrid, and electric vehicles, which use Li-ion batteries as the energy storage medium. According to a market survey, the Li-ion battery market will reach USD45 billion in the in the next few years [2].

Accidents, some of them fatal, have accompanied the growing popularity and usage of Li-ion batteries [37; 51]. More recently, cell phones catching on fire has been widely reported, and as a consequence, the manufacturer had to have a worldwide recall [52; 53]. These accidents are attributed to failure of Li-ion batteries, which results in a fire, often leading to an explosion [54; 55], and usually happens because of internal short circuits, which leads to thermal runaway. Li-ion batteries are made of structure of positive electrode-plastic separator-negative electrode, wound together like a jellyroll, permeated with an electrolyte and enclosed in a metallic shell. The plastic separator has a relative low melting point, $\sim$130°C. During operation, electrochemical reactions generate heat, and at certain electrical configurations or high operating rates, temperature goes on increasing, leading to a failure. Research has

shown that most of the heat is generated at the core of the cell, and needs to conduct across the jellyroll, through the metal case to the outer surrounding. This conduction heat transfer is not efficient, since each interface in the jellyroll provides a thermal interfacial resistance. For efficient modeling and safety studies, it is important to characterize this interfacial resistance. Specifically, it is found that the final layer of the jellyroll which is in contact with the case is the plastic separator. This interface is the ultimate barrier which may limit heat transfer from the cell to the surrounding.

Here, a methodology for measuring the effective thermal conductivity of the electrodes is presented, along with measurements of thermal conductance across the separator-case interface, at various temperatures and pressures. A miniaturized version of the conventional reference bar method is integrated with infrared (IR) microscopy, to spatially resolve the interfacial temperature drops or the contact resistance from the intrinsic thermal conductivity of the specimen (see Chapter 2) [18;19]. Commercial cylindrical 18650 batteries have been dissected to harvest the jellyrolls, and electrodes have been separated and the electrolyte is washed off to perform experiments in air. Experiments to measure thermal conductance across the separator-case interface have been performed for 35-120 °C, between a pressure range of 0.1-0.25MPa for each case temperature. The first measurements of this crucial interface have been reported, and the mean conductance across all pressures and temperatures is measured to be 670 W/(m^{2}K), with a standard deviation of 275 W/(m^{2}K). In these measurements and between these temperature and pressure ranges, no statistically significant temperature or pressure variation is seen. Since the actual contact pressure at the jellyroll-case interface is unknown, there is a need to perform experiments with actual batteries, without harvesting the electrodes. Chapter 3 develops a methodology for performing cylindrical battery level measurements for measuring thermal conductivity and interfacial conductance of 18650 batteries. A test rig is designed, validated and manufactured. Since the electrolyte degrades in air, initial experiments are performed with dry batteries constructed with electrodes bought from MTI Corporation. In a cylindrical configuration, the thermal conductivity of the battery stack

is measured to be 0.24 W/m/K, as compared to the 0.27 W/m/K in a linear configuration.

The active material of the Li-ion battery electrodes is porous, *e.g.*, the anode consists of a thin copper current collector coated with a graphite layer. Characterizing heat conduction in such granular media is critical to the design of energy storage applications. Past work has shown that the application of external mechanical forces on a packed granular bed enhances its effective thermal conductivity [43; 45]. To this effect, a test rig capable of simultaneously applying mechanical shear and a temperature gradient across a granular bed is designed and manufactured. This rig is validated using standard reference materials. Thermal conductivity measurements are performed before and after shearing, and the change in thermal conductivity is calculated. Challenges, such as convection losses, faced during the validation phase are addressed by trying to build a convection shielding box, and a retrofitted vacuum chamber. This work lays a foundation for understanding the micro structural rearrangements that occur due to external forces on granular media, and could help in developing custom composites with tailored thermal properties.

5.2 Future Work

Lithium-ion batteries are hermetically sealed, and as they go through operating cycles, the jellyroll tends to swell, and the operating pressures increase. Although measurements conducted in this research did not show a significant trend with pressure or temperature, extreme pressure ranges might need to be investigated to measure the pressure dependence of thermal conductance. Similarly, the impact of failure (melting/short circuit) on interfacial conductance could be investigated, when the plastic separator melts and the positive and negative electrodes come in electrical contact with each other.

Due to the challenges with exposing and working with the battery electrolyte in air, the measurements performed in this work dealt with either dry batteries or

electrodes without an electrolyte. With the procedure of cutting active batteries open in place, a vacuum chamber, or an inert gas chamber needs to be designed, with a infrared transmitting window, with feedthroughs for thermocouple and heater leads, to enable measurements with the electrolyte inside the battery. This design of the test rig, coupled with high resolution IR imaging will provide crucial data and insights into the thermal transport across the battery electrodes, and help in designing safer batteries of a larger capacity for the future.

LIST OF REFERENCES

LIST OF REFERENCES

[1] Strong growth ahead for lithium ion battery market. https://epsnews.com/2016/07/06/lithium-ion-battery-market/, Accessed: 2016-10-10.

[2] Swelling global lithium market forecasted to top usd46 billion by 2022. http://www.releasewire.com/press-releases/swelling-global-lithium-market-forecasted-to-top-46-billion-by-2022-company-announces-acquisition-of-1200-acres-of-nevada-lithium-mining-project-681935.htm, Accessed: 2016-10-10.

[3] S. A. Hallaj, H. Maleki, J.S. Hong, and J.R. Selman. Thermal modeling and design considerations of lithium-ion batteries. *Journal of Power Sources*, 83(1):1–8, 1999.

[4] M. Armand and J. M. Tarascon. Building better batteries. *Nature*, 451(7179):652–657, 2008.

[5] J. B. Goodenough and K. S. Park. The Li-ion rechargeable battery: A perspective. *Journal of the American Chemical Society*, 135(4):1167–1176, 2013.

[6] University of Washington. Lithium Ion Battery what is a lithium ion battery and how does it work, 2016. http://www.cei.washington.edu/education/science-of-solar/battery-technology/.

[7] H. Maleki, S. A. Hallaj, J. R. Selman, R. B. Dinwiddie, and H. Wang. Thermal Properties of Lithium-Ion Battery and Components. *Journal of The Electrochemical Society*, 146(3):947, 1999.

[8] Q. Wang, P. Ping, X. Zhao, G. Chu, J. Sun, and C. Chen. Thermal runaway caused fire and explosion of lithium ion battery. *Journal of Power Sources*, 208:210–224, 2012.

[9] C. Forgez, D. Dinh, G. Friedrich, M. Morcrette, and C. Delacourt. Thermal modeling of a cylindrical LiFePO4/graphite lithium-ion battery. *Journal of Power Sources*, 195(9):2961–2968, 2010.

[10] S.J. Drake, D.A. Wetz, J.K. Ostanek, S.P. Miller, J.M. Heinzel, and A. Jain. Measurement of anisotropic thermophysical properties of cylindrical Li-ion cells. *Journal of Power Sources*, 252:298–304, 2014.

[11] B. Scrosati and J. Garche. Lithium batteries: Status, prospects and future. *Journal of Power Sources*, 195(9):2419–2430, 2010.

[12] V. Vishwakarma, C. Waghela, Z. Wei, R. Prasher, S. C. Nagpure, J. Li, F. Liu, C. Daniel, and A. Jain. Heat transfer enhancement in a lithium-ion cell through improved material-level thermal transport. *Journal of Power Sources*, 300:123–131, 2015.

[13] Y. Saito, K. Kanari, and K. Takano. Thermal studies of a lithium-ion battery. *Journal of Power Sources*, 68(2):451–454, 1997.

[14] K. Shah, V. Vishwakarma, and A. Jain. Measurement of Multiscale Thermal Transport Phenomena in Li-ion Cells: A Review. *Journal of Electrochemical Energy Conversion and Storage*, (c), 2016.

[15] S.J. Drake, M. Martin, D.A. Wetz, J.K. Ostanek, S.P. Miller, J.M. Heinzel, and A. Jain. Heat generation rate measurement in a Li-ion cell at large C-rates through temperature and heat flux measurements. *Journal of Power Sources*, 285:266–273, 2015.

[16] K. Shah, C. McKee, D. Chalise, and A. Jain. Experimental and numerical investigation of core cooling of Li-ion cells using heat pipes. *Energy*, 113:852–860, 2016.

[17] R. Ponnappan and T.S. Ravigururajan. Contact thermal resistance of Li-ion cell electrode stack. *Journal of Power Sources*, 129(1):7–13, 2004.

[18] ASTM Standard. D5470-12. *Standard Test Method for Thermal Transmission Properties of Thermally Conductive Electrical Insulation Materials, West Conshohocken, PA: ASTM International*, 2012.

[19] M. T. Barako, Y. Gao, Y. Won, A. M. Marconnet, M. Asheghi, and K. E. Goodson. Reactive metal bonding of carbon nanotube arrays for thermal interface applications. *IEEE Transactions on Components, Packaging and Manufacturing Technology*, 4(12):1906–1913, 2014.

[20] A. M. Marconnet, N. Yamamoto, M. A. Panzer, B. L. Wardle, and K. E. Goodson. Thermal conduction in aligned carbon nanotube-polymer nanocomposites with high packing density. *ACS nano*, 5(6):4818–25, Jun 2011.

[21] K. Striebel, J. Shim, A. Sierra, H. Yang, X. Song, R. Kostecki, and K. McCarthy. The development of low cost LiFePO4-based high power lithium-ion batteries. *Journal of Power Sources*, 146(1):33–38, 2005.

[22] C. Y. Jhu, Y.W. Wang, C.M. Shu, J.C. Chang, and H. C. Wu. Thermal explosion hazards on 18650 lithium ion batteries with a VSP2 adiabatic calorimeter. *Journal of Hazardous Materials*, 192(1):99–107, 2011.

[23] Li-ion battery cathode - aluminum foil double side coated by lifepo4. `http://www.mtixtl.com/Li-IonBatteryCathode-AluminumfoildoublesidecoatedbyLiFePO4241mm.aspx`, Accessed: 2016-10-22.

[24] Li-ion battery anode -copper foil single side coated by cms graphite. `http://www.mtixtl.com/Li-IonBatteryAnode-CopperfoilsinglesidecoatedbyCMSGraphite241mm-1.aspx`, Accessed: 2016-10-22.

[25] Li-ion battery separator film. `http://www.mtixtl.com/separatorfilm-EQ-bsf-0025-60C.aspx`, Accessed: 2016-10-22.

[26] D. Collins. Handbook of batteries and fuel cells By David Linden, published by McGraw-Hill Book Company GmbH., Hamburg, F.R.G., 1984; 1024 pp.; price DM 258.80. *Journal of Power Sources*, 17(4):379–384, 1986.

[27] J. Jeevarajan. Safety Limitations Associated with Commercial 18650 Lithium-ion Cells. 2010.

[28] C. Menictas, M. Skyllas-Kazacos, and T. M. Lim. *Advances in batteries for medium- and large- scale energy storage*.

[29] J.S. Hong, H. Maleki, S. Al Hallaj, L. Redey, and J.R. Selman. Electrochemical-calorimetric studies of lithium-ion cells. *Journal of the Electrochemical Society*, 145(5), 1998.

[30] C. Hendricks, N. Williard, S. Mathew, and M. Pecht. A failure modes, mechanisms, and effects analysis (FMMEA) of lithium-ion batteries. *Journal of Power Sources*, 297:113–120, 2015.

[31] M. J. Armstrong, C. O'Dwyer, W. J. Macklin, and J. D. Holmes. Evaluating the performance of nanostructured materials as lithium-ion battery electrodes. *Nano Research*, 7(1):1–62, 2014.

[32] C.E. Thomas. Fuel cell and battery electric vehicles compared. *International Journal of Hydrogen Energy*, 34(15):6005–6020, 2009.

[33] J. Zhang, B. Wu, Z. Li, and J. Huang. Simultaneous estimation of thermal parameters for large-format laminated lithium-ion batteries. *Journal of Power Sources*, 259:106–116, 2014.

[34] R. Spotnitz and J. Franklin. Abuse behavior of high-power, lithium-ion cells. *Journal of Power Sources*, 113(1):81–100, 2003.

[35] J. Cho, M. D. Losego, H. G. Zhang, H. Kim, J. Zuo, I. Petrov, D. G. Cahill, and P. V. Braun. Electrochemically tunable thermal conductivity of lithium cobalt oxide. *Nature communications*, 5(May):4035, 2014.

[36] H. Maleki, J. R. Selman, R. B. Dinwiddie, and H. Wang. High thermal conductivity negative electrode material for lithium-ion batteries. *Journal of power sources*, 94(1):26–35, 2001.

[37] Q. Wang, P. Ping, X. Zhao, G. Chu, J. Sun, and C. Chen. Thermal runaway caused fire and explosion of lithium ion battery. *Journal of power sources*, 208:210–224, 2012.

[38] W. Zhang, X. Zhang, C. Wang, G. Yu, and C. Yang. Experimental and computational research on the thermal conductivities of li/socl2 batteries. *Journal of The Electrochemical Society*, 161(5):A675–A681, 2014.

[39] Chemours.com. Teflon chemours, 2016. `https://www.chemours.com/Teflon/en_US/`.

[40] M. Pilsworth and H. Robinson. The Thermal Conductivity of Natural Rubber, 1971.

[41] Y. Sheng, C. R. Fell, Y. K. Son, B. M. Metz, J. Jiang, and B. C. Church. Effect of Calendering on Electrode Wettability in Lithium-Ion Batteries. *Frontiers in Energy Research*, 2(December):1–8, 2014.

[42] M. Ebner, D. W. Chung, R. E. García, and V. Wood. Tortuosity anisotropy in lithium-ion battery electrodes. *Advanced Energy Materials*, 4(5):1–6, 2014.

[43] K. C. Smith and T. S. Fisher. Conduction in Jammed Systems of Tetrahedra. *Journal of Heat Transfer*, 135(8):081301, 2013.

[44] R. J. Mehta, Y. Zhang, C. Karthik, B. Singh, R. W. Siegel, T. Borca-Tasciuc, and G. Ramanath. A new class of doped nanobulk high-figure-of-merit thermoelectrics by scalable bottom-up assembly. *Nature materials*, 11(3):233–40, mar 2012.

[45] I. Srivastava and T. S. Fisher. Microstructure and thermal conductivity modeling of granular nanoplatelet assemblies. *32nd International Thermal Conductivity Conference and 20th International Thermal Expansion Symposium*, pages 44–52, 2014.

[46] B. Van and R. Divigalpitiya. Effect of Calendering LiFePO4 Electrodes. *Journal of the Electrochemical Society*, 159(11):A1791–A1795, 2012.

[47] H. Zheng, L. Tan, G. Liu, X. Song, and V. S. Battaglia. Calendering effects on the physical and electrochemical properties of Li[Ni1/3Mn1/3Co1/3]O2 cathode. *Journal of Power Sources*, 208:52–57, 2012.

[48] P. Peng and F. Jiang. Thermal safety of lithium-ion batteries with various cathode materials: A numerical study. *International Journal of Heat and Mass Transfer*, 103:1008–1016, 2016.

[49] X. Feng, L. Lu, M. Ouyang, J. Li, and X. He. A 3D thermal runaway propagation model for a large format lithium ion battery module. *Energy*, 115:194–208, 2016.

[50] F. Zheng, J. Jiang, B. Sun, W. Zhang, and M. Pecht. Temperature dependent power capability estimation of lithium-ion batteries for hybrid electric vehicles. *Energy*, 113:64–75, 2016.

[51] Mashable. Tesla fire, 2016. `http://mashable.com/2016/11/04/fatal-tesla-crash-batteries-fires/#c9uziRsWwaqt`.

[52] Cnet. Samsung Note 7 fire, 2016. `https://www.cnet.com/news/why-is-samsung-galaxy-note-7-exploding-overheating/`.

[53] British Broadcasting Corporation. Fixed Samsung Note 7 Catches Fire on a Plane fire, 2016. `http://www.bbc.com/news/technology-37570100`.

[54] J. M. Tarascon and M. Armand. Issues and challenges facing rechargeable lithium batteries. *Nature*, 414(6861):359–67, 2001.

[55] P.G. Balakrishnan, R. Ramesh, and T. Prem Kumar. Safety mechanisms in lithium-ion batteries. *Journal of Power Sources*, 155(2):401–414, 2006.

APPENDIX

APPENDIX A. FABRICATION OF THE COUETTE CELL

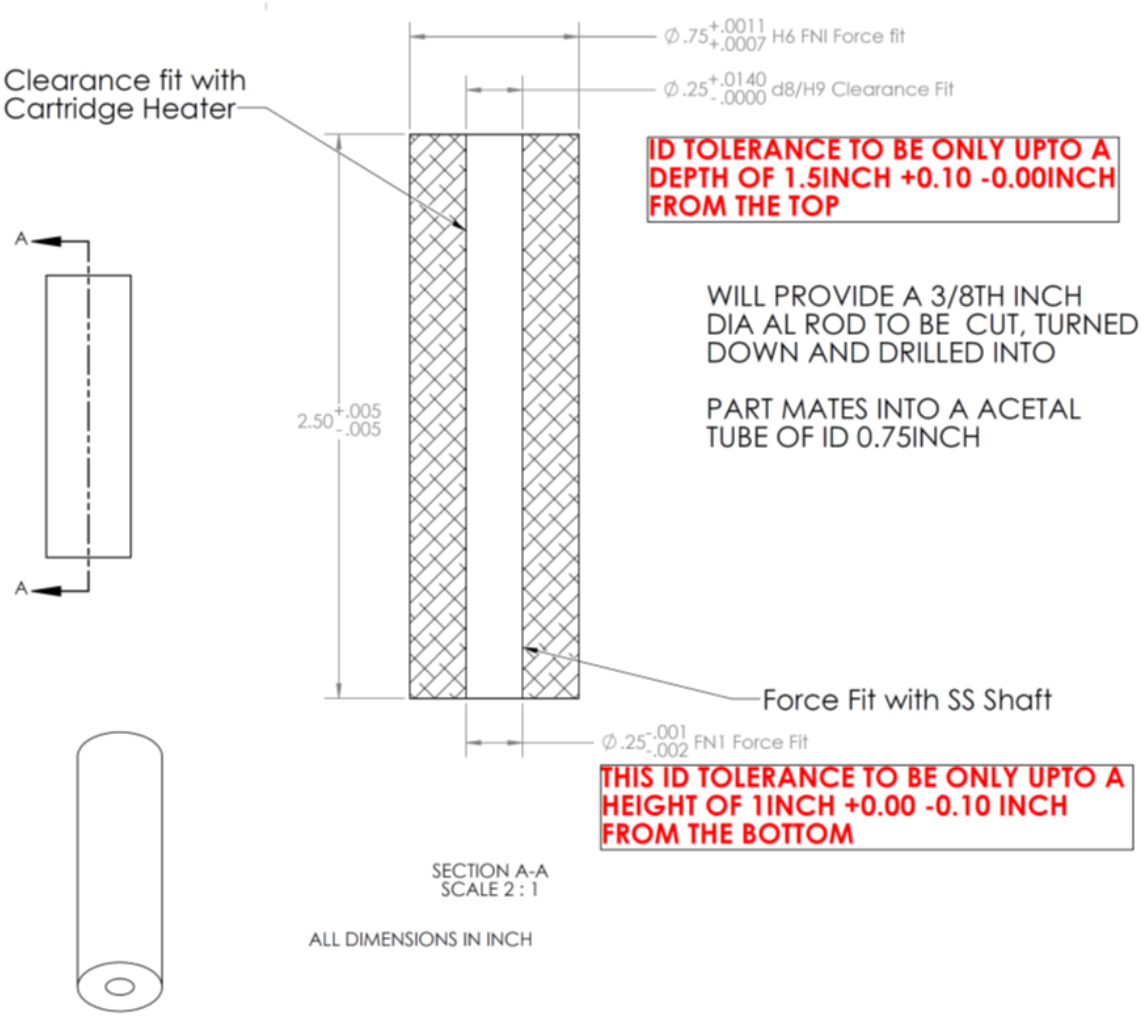

Figure A.1. A representative part drawing of the hollow inner cylinder which houses the heater in the top half, and the shaft in the bottom half (heater and shaft not shown in this drawing). The nominal diameter of the hole is 1/4 inch, and the type of fit, i.e clearance fit for the heater and an interference fit for the shaft is specified on the part drawing.

Figure A.1 shows a representative part drawing used for manufacturing one of the the components, the 'Inner Cylinder', which corresponds to call out 2 in Figure 4.2. Although the nominal size of the hole is 1/4 inch, this part houses a cylindrical cartridge heater on the top end, and a 1/4 inch shaft on the bottom end. The heater needs to have a clearance fit inside the hole, since it expands during operation. Hence, positive unilateral tolerances are provided for the part of the hole that houses the heater, to provide a d8/H9 Clearance Fit. On the bottom the hole, negative unilateral tolerances are specified to ensure a FN1 Force Fit with the shaft. Both the shaft and the heater are not shown in Figure A.1.

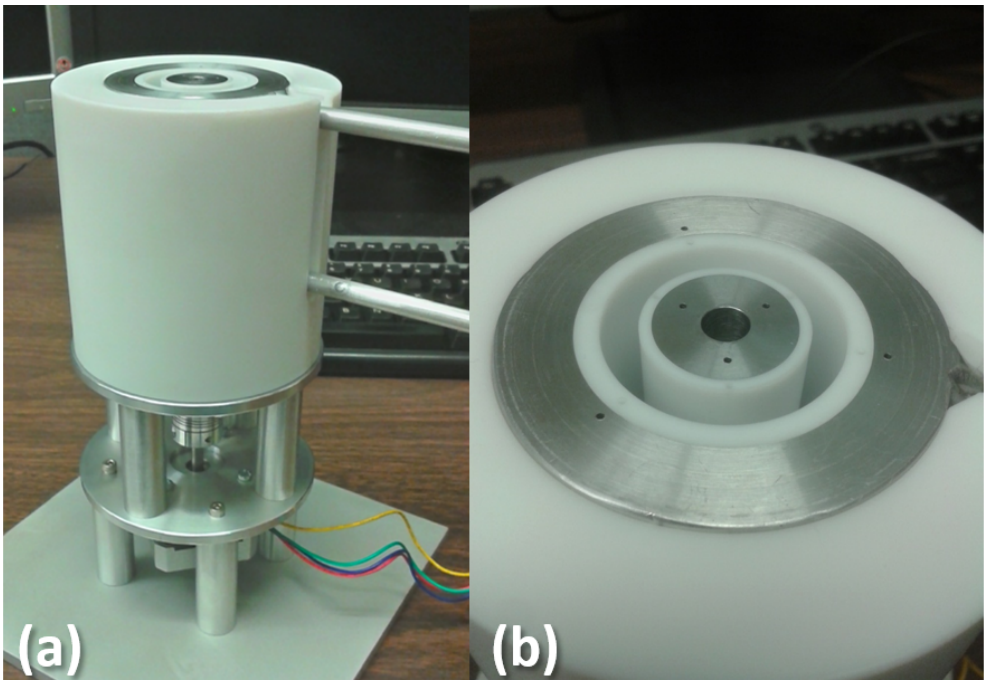

Figure A.2. (a) The manufactured Couette Cell, standing on the support assembly and DC motor at the bottom. The two pipes coming off from the sides are the inlet and outlet of the heat exchanger, which flows coolant through the outer cylinder. (b) A close-up of the top surface of the Couette Cell, which shows the inner Aluminum cylinder with the hole for the cartridge heater, and the annular cavity for the granular media. The small holes are for inserting 30 Gauge T-type thermocouples for secondary temperature measurements. A part of this surface, which includes the inner reference, sample and outer reference, is imaged using the infrared microscope.

To create a temperature gradient, while the hot side temperature is maintained by the cartridge heater embedded in the inner cylinder, the cold side temperature on the outer cylinder is maintained by flowing a cold heat transfer fluid through the helical heat exchanger which is integrated with the outer cylinder. Figure A.3(a) shows the internal grooves cut on a thick walled Aluminum cylinder, which when press fitted with another Aluminum tube, functions like a heat exchanger. The groove is a square channel of side 1/8 inch. Pressure drop calculations, shown in A.3(b) show that the pressure drop will be less than the highest operating pressure of the heat transfer fluid circulator.

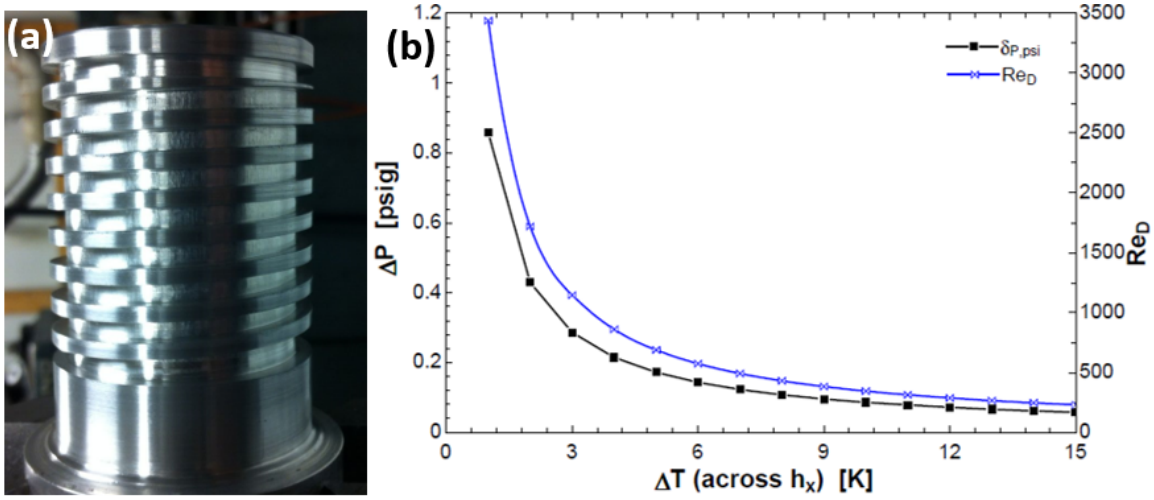

Figure A.3. (a) The heat exchanger channels (helical grooves) cut on a thick walled Aluminum cylinder. Another thin walled Aluminum tube is press fitted over this grooved cylinder, and an inlet and outlet tube is connected to the bottom and top of the grooves, creating a closed loop heat exchanger. (b) The calculated pressure drop as a function of Reynolds number. This exercise was performed to measure the circulator pump requirement.

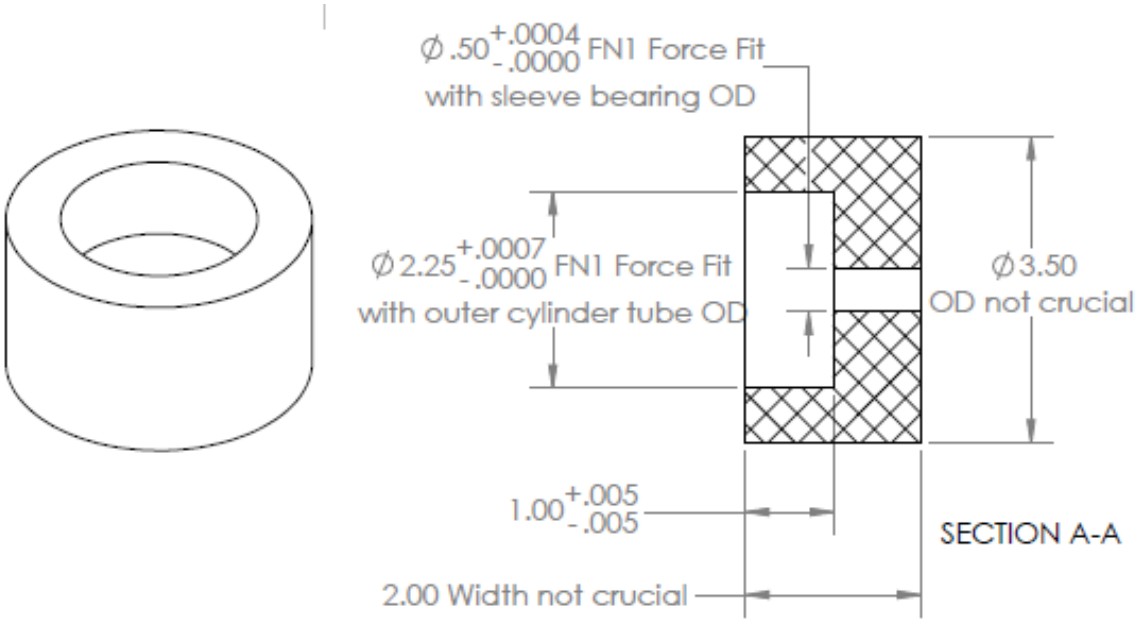

Figure A.4. The base fixture supports the assembly of concentric cylinders of the Couette Cell, as well as insulating the outer surface of the heat exchanger. The hole at the base of the fixture houses a sleeve bearing, which aligns the shaft of motor with the inner cylinder. This support is machined from a rod of PTFE.

VITA

VITA

Aalok Gaitonde is a graduate student at Purdue University, since Fall 2014. He has been a graduate assistant with the Marconnet Thermal and Energy Conversion Laboratory, School of Mechanical Engineering, and his research was Li-ion battery thermal characterization, and developing a methodology to experimentally characterize heat transport in packed granular media. He has a Bachelors degree in Mechanical Engineering from the University of Pune, India, and before getting into grad school, he worked at IIT Bombay as a Research Assistant.

Personal Webpage: `https://www.linkedin.com/in/aalokgaitonde`